Numerical Simulation of Ca^{2+} "Sparks" in Skeletal Muscle

Yu-Hua Jiang,*† Michael G. Klein,* and Martin F. Schneider*

*Department of Biochemistry and Molecular Biology, University of Maryland School of Medicine, Baltimore, Maryland 21201, and †Department of Mechanical Engineering, College of Engineering, University of Maryland Baltimore County, Baltimore, Maryland 21250, U.S.A.

ABSTRACT A three dimensional (3D) model of Ca^{2+} diffusion and binding within a sarcomere of a myofibril, including Ca^{2+} binding sites troponin, parvalbumin, sarcoplasmic reticulum Ca^{2+} pump, and fluorescent Ca^{2+}-indicator dye (fluo-3), was developed to numerically simulate laser scanning confocal microscope images of Ca^{2+} "sparks" in skeletal muscle. Diffusion of free dye (D), calcium dye (CaD), and Ca^{2+} were included in the model. The Ca^{2+} release current was assumed to last 8 ms, to arise within 4×10^{-5} μm^3 at the triad and to be constant during release. Line scan confocal fluorescence images of Ca^{2+} sparks were simulated by 3D convolution of the calculated distribution of CaD with a Gaussian kernel approximating the point spread function of the microscope. Our results indicate that the amplitude of the simulated spark is proportional to the Ca^{2+} release current if all other model parameters are constant. For a given release current, the kinetic properties and concentrations of the binding sites and the diffusion parameters of D, CaD, and Ca^{2+} all have significant effects on the simulated Ca^{2+} sparks. The simulated sparks exhibited similar amplitudes and temporal properties, but less spatial spread than experimentally observed sparks.

DEFINITION OF SYMBOLS

Symbols in the text surrounded by brackets [ ] represent concentrations of the indicated species.

Ca^{2+} = Calcium
CaATP = Calcium ATP
CaD = Calcium dye
CaP = Calcium pump
CaPARV = Calcium parvalbumin
CaTN = Calcium troponin
d = Depth of the computational domain
D = Dye
D_{ATP} = Diffusion coefficient of ATP
D_C = Diffusion coefficient of Ca^{2+}
D_{CaATP} = Diffusion coefficient of CaATP
D_{CaD} = Diffusion coefficient of CaD
D_D = Diffusion coefficient of D
D_{MgATP} = Diffusion coefficient of MgATP
F = Fluorescence signal
F_0 = Resting fluorescence signal
FDHM = Full duration at half maximum
FWHM = Full width at half maximum
h = Height of the computational domain
I = Magnitude of Ca^{2+} current
$k_{off,CaATP}$ = Backward rate constant for Ca^{2+} and ATP
$k_{off,CaD}$ = Backward rate constant for Ca^{2+} and D
$k_{off,CaP}$ = Backward rate constant for Ca^{2+} and pump
$k_{off,CaPARV}$ = Backward rate constant for Ca^{2+} and parvalbumin
$k_{off,CaTN}$ = Backward rate constant for Ca^{2+} and troponin
$k_{off,MgATP}$ = Backward rate constant for Mg^{2+} and ATP
$k_{off,MgPARV}$ = Backward rate constant for Mg^{2+} and parvalbumin
$k_{on,CaATP}$ = Forward rate constant for Ca^{2+} and ATP
$k_{on,CaD}$ = Forward rate constant for Ca^{2+} and D
$k_{on,CaP}$ = Forward rate constant for Ca^{2+} and pump
$k_{on,CaPARV}$ = Forward rate constant for Ca^{2+} and parvalbumin
$k_{on,CaTN}$ = Forward rate constant for Ca^{2+} and troponin
$k_{on,MgATP}$ = Forward rate constant for Mg^{2+} and ATP
$k_{on,MgPARV}$ = Forward rate constant for Mg^{2+} and parvalbumin
k_P = Rate constant for SR Ca^{2+} pump
l = Length of the computational domain
L = Ca^{2+} leak from SR
LSCI = Laser scanning confocal imaging
LSCM = Laser scanning confocal microscope
Mg^{2+} = Magnesium
MgATP = Magnesium ATP
MgPARV = Magnesium parvalbumin
MPE = Maximum percentage error
MSPE = Mean square percentage error
P = SR Ca^{2+} pump
PARV = Parvalbumin
PSF = Point spread function
RF = Reducing factor of diffusion coefficients at SR
R_r = Calcium release rate at the source
RMSPE = Square root of MSPE
RTime = Rise time, time to go from 10 to 90% of peak value
SR = Sarcoplasmic reticulum

Received for publication 15 July 1998 and in final form 26 July 1999.

Address reprint requests to Dr. Martin F. Schneider, Dept. of Biochemistry and Molecular Biology, University of Maryland School of Medicine, 108 N. Greene St., Baltimore, MD 21201. Tel.: 410-706-7812; Fax: 410-706-8297; E-Mail: mschneid@umaryland.edu.

0006-3495/99/11/2333/25 $2.00

Str = Starting values
TN = Troponin
V = SR Ca^{2+} pump transport
V_0 = Resting SR Ca^{2+} pump transport
Δt = Time step size
Δx = Spatial step size in x direction
Δy = Spatial step size in y direction
Δz = Spatial step size in z direction

INTRODUCTION

Since the detection and report of Ca^{2+} "sparks" in cardiac (Cheng et al., 1993) and skeletal muscle (Tsugorka et al., 1995; Klein et al., 1996), considerable effort has been devoted to the investigation of the mechanism underlying the observed sparks. However, it is not obvious which aspects of Ca^{2+} sparks are determined by the activity pattern of the SR Ca^{2+} channel or channels which underly the generation of sparks, and which properties are determined by the diffusion and Ca^{2+} binding kinetics of both the intrinsic binding sites in the fiber and the Ca^{2+} indicator dye. Numerical simulation is a feasible approach to evaluate these factors in studying the Ca^{2+} movement underlying the sparks.

The complete simulation of Ca^{2+} sparks, as measured experimentally using laser scanning confocal microscopy in a skeletal muscle fiber, consists of two main parts. The first part is the simulation of the Ca^{2+}-dye formation process and its spatiotemporal distribution by a diffusion and binding model. The second part is the simulation of the imaging process based on the results from the first part and the optical properties of the confocal microscope. This entire process is actually in close analogy to the experimental observation of the sparks, in which, first, the sparks are produced by the release and spread of Ca^{2+} from the Ca^{2+} release channel source in the junctional SR and the reactions of Ca^{2+} with fluo-3 and other myoplasmic Ca^{2+} binding sites. The change in Ca^{2+} dye is monitored as a change in fluorescence by the LSCM. In the present article, we first simulated the spread of Ca^{2+} dye due to the diffusion and binding processes, then simulated the image acquisition by the LSCM by convolving an approximation of the theoretical PSF of the LSCM with the simulated data from the diffusion and binding model.

Our model of diffusion and binding is a combination of structural domain configuration and functional equation formulation. The model was based on the physical structure of a sarcomere within a myofibril of a skeletal muscle fiber. The mathematical equation system was formulated on mass diffusion theory and chemical reaction kinetics. The following aspects represent the most important developments of the present three-dimensional (3D) simulation model from other published models of Ca^{2+} movements underlying Ca^{2+} sparks: 1) the diffusion of Ca^{2+} dye (D) and Ca dye (CaD) were included in the starting simulation; 2) several main Ca^{2+} binding sites were treated separately instead of being treated as a single lumped ligand (Blatter et al., 1997; Pratusevich and Balke, 1996), and the reaction rate constants were chosen from literature or experimental results; 3) the distributions of the binding sites were modeled in close analogy to the biological structure; 4) the computational domain was discretized into a graded network for the finite difference solution of the differential equation system, which ensured the necessary accuracy near the Ca^{2+} release source and reduced the computation load far from the source; 5) the numerical solutions of the diffusion processes of both an instantaneous source and a continuous source were verified by the comparison with the analytical solutions of the same processes under the condition of no binding reactions.

The main applications of the model have been the simulation of experimentally measured sparks; the comparison of sparks viewed at different positions relative to the Ca^{2+} source; and the investigation of the effects of changes in the Ca^{2+} release current source and of changes in the parameters for the Ca^{2+} binding sites, in the diffusion coefficients of D and CaD and in Ca^{2+} dye kinetics and concentration on the properties of the sparks. With appropriate sets of parameter values, the simulated Ca^{2+} sparks presented here reproduce many features of the amplitude and temporal properties of Ca^{2+} sparks recorded experimentally from frog skeletal muscle fibers (e.g., Lacampagne et al., 1996, 1998). However, the spatial spread of the simulated sparks, calculated as the spatial FWHM, was consistently less than experimentally measured values.

METHODS

The diffusion and binding model

The central aspect of our simulation was the mass diffusion theory. The general equation for diffusion of substance A in a homogeneous and isotropic medium is (Crank, 1975)

$$\frac{\partial[\mathrm{A}]}{\partial t} = D_{\mathrm{A}}\nabla^2[\mathrm{A}], \tag{1}$$

where ∇^2 is the Laplacian operator. D_A is the diffusion coefficient of substance A and [A] is its concentration. This is a parabolic partial differential equation, the numerical solution of which is to track the time evolution of variable [A]. [A] is implicitly understood to be a function of time t and spatial coordinates x, y, and z, i.e., [A](t, x, y, z), but the time and space coordinates are not explicitly stated to simplify the notation. In Cartesian coordinates, $\nabla^2 = (\partial^2/\partial x^2 + \partial^2/\partial y^2 + \partial^2/\partial z^2)$.

When the diffusion process is involved with chemical reactions, the general Eq. 1 for diffusion, with the diffusing substance A given by free Ca^{2+} as in this study, is (cf., Cannel and Allen, 1984)

$$\frac{\partial[\mathrm{Ca}^{2+}]}{\partial t} = D_{\mathrm{C}}\nabla^2[\mathrm{Ca}^{2+}] - F([\mathrm{Ca}^{2+}], t), \tag{2}$$

where

$$F([\mathrm{Ca}^{2+}], t) = \sum \frac{\mathrm{d}[\mathrm{Ca}B_{\mathrm{i}}]}{\mathrm{d}t} \tag{3}$$

represents the effect of chemical reactions on the rate of change of $[Ca^{2+}]$. B_i represent different binding sites and buffers. In the present study, we use the term "site" to indicate non- or slowly diffusible reactants binding Ca^{2+}

and the term "buffer" to indicate diffusible reactants binding Ca^{2+}. Eq. 2 is also the general equation used in the present study from which the structural domain configuration and the functional equation systems were developed.

Structural domain configuration

The first step in building our model was to define the elementary building block in the model. Because a myofibril is the contractile element of a skeletal muscle cell and is composed of repeating contractile units, or sarcomeres, it seemed reasonable to take a single sarcomere as the elementary block in our model. The shape of this elementary block was chosen to be rectangular for computational convenience.

The width of the cross section of the elementary sarcomere block was set as 1.0 μm, close to the average width of a single myofibril. From the fact that skeletal muscle fibers were usually stretched to 3.8 $\sim$ 4.2 μm per sarcomere to completely eliminate contraction (Klein et al., 1991) in the Ca^{2+} transient experiments performed in our laboratory, the length of the elementary block was set as 4.0 μm. The size of the whole simulation domain was determined by the average sizes of the sparks in skeletal muscle. Because the mean spatial FWHM of Ca^{2+} sparks in skeletal muscle is approximately 1.5 μm (Lacampagne et al., 1996, 1998), the shortest width of the simulation domain was chosen to be 3.0 μm, or three myofibrils wide. A space of twelve neighboring elementary sarcomere blocks with two sarcomeres long (x), three myofibrils deep (y), and four myofibrils high (z), which has the sizes of 8.0 μm $\times$ 3.0 μm $\times$ 4.0 μm, will satisfy this condition (Fig. 1 *A*). The height z of the domain was made a little larger than that of the depth y because the z resolution of the confocal microscope in the z dimension is roughly half that in the x or y dimensions, and for the purpose of investigating the line scan images from out-of-focus sparks. The actual size of the computational domain (Fig. 1 *B*) was further reduced from above sizes by considering the location of the Ca^{2+} release source and the symmetries around the source. Experimental evidence indicated that the local elevations of $[Ca^{2+}]$, Ca^{2+} sparks, during depolarization as well as the spontaneous events originated at the triads (Klein et al., 1996; Schneider and Klein, 1996), which is the junction of T-tubule and two terminal cisterni on both sides. We therefore assumed that the point source of Ca^{2+} release was located between the two central sarcomeres of the 12-sarcomere space and at the Z disk separating the 2 one-sarcomere sections (Fig. 1 *A*). In other words, the Ca^{2+} release source was located at the center of the simulation domain. Diffusion and binding of Ca^{2+} from the source into any one of the eight sub-domains was

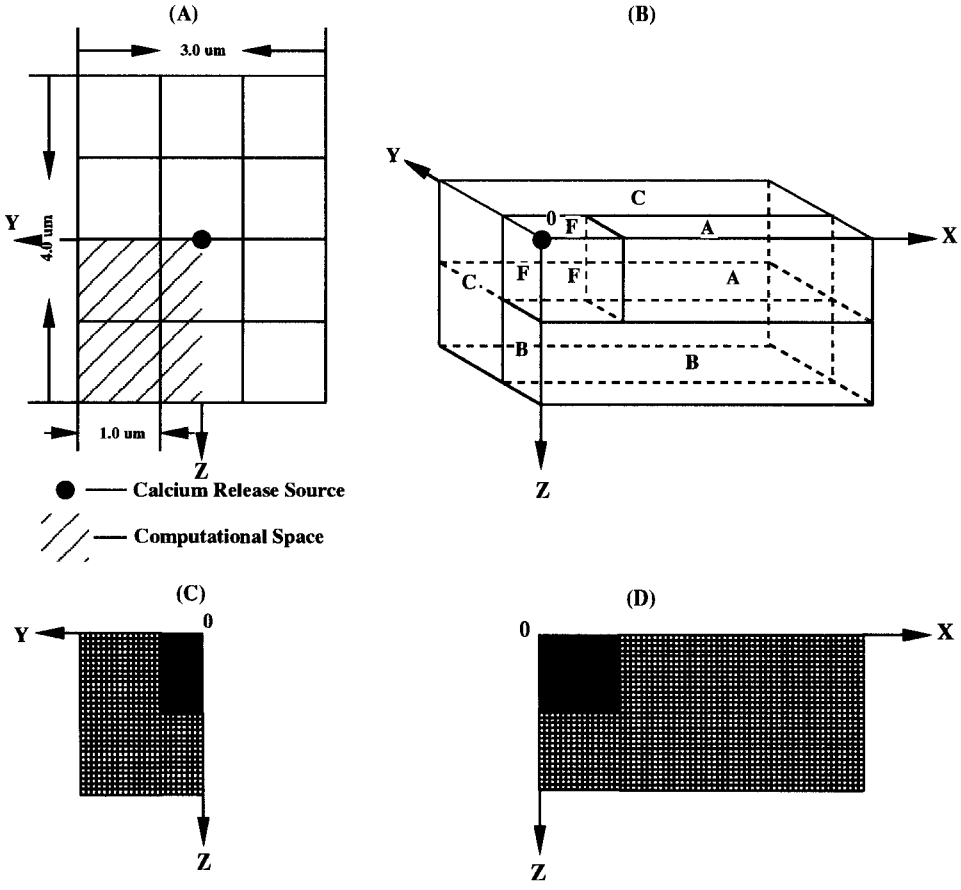

FIGURE 1 Schematic representation of the model structure. (*A*) The central cross section of the simulation domain, which cuts the entire simulation domain into two one-sarcomere sections. The fiber and myofibril axis is perpendicular to the plane shown. The whole simulation domain composed of 12 neighboring elementary sarcomere blocks with four-sarcomere deep (vertical), three-sarcomere wide (horizontal), and two-sarcomere long (not shown), which has the sizes of 4.0 $\times$ 3.0 $\times$ 8.0 μm. The cross section and the space of the computational domain are ¼ and ⅛ of those of the simulation domain, respectively. (*B*) The 3D view of the computational domain, which consists of a fine network block F and three coarse network blocks A, B, and C. Block F has 16,337 cubic voxels of the size of 0.0333^3 μm^3 each. Blocks A, B, and C have 6480, 8784, and 31,232 cubic voxels, respectively, and the size of their voxels is 0.0666^3 μm^3 each. The simulation results in coarse blocks A, B, and C will be interpolated and the total numbers of voxels in the entire computational domain are 62,833 and 373,527 before and after the interpolation, respectively. The x axis is along the long axis of the computational domain, and the y and z axes are the horizontal and vertical short axes of the computational domain. (*C*) and (*D*) The first Y–Z and X–Z planes of the computational domain.

assumed to be symmetric. Therefore, the computation was restricted to one-eighth of the simulation domain as shown in the shaded area in Fig. 1 *A* and the cut off part in Fig. 1 *B*.

In previous simulations of Ca^{2+} movements, the Ca^{2+} binding components were assumed to be uniformly distributed in the cytoplasm (Blatter et al., 1997) or modeled as a lumped single immobile buffer (Pratusevich and Balke, 1996; Blumenfeld et al., 1992; Kargacin, 1994; Kargacin and Fay, 1991). To achieve a more realistic simulation, three main Ca^{2+} binding sites, troponin, parvalbumin, and the SR Ca^{2+} pump, in addition to the Ca^{2+} indicator, fluo-3 (D), were considered explicitly in our model. Ca^{2+} leak from the SR and the Ca^{2+} transport back to the SR were also considered in the model. In contrast to modeling all the binding sites as uniformly distributed throughout the cytoplasm, we treated different binding sites differently according to the structure of the sarcomere. Parvalbumin was considered as uniformly distributed in the whole sarcomere, whereas troponin was modeled as being distributed on the thin filaments in the sarcomere, which were located in the 1.0-μm long sections on either sides of the *Z*-disk at the two ends of the elementary block. The Ca^{2+} pump sites were assumed to be distributed on the SR surrounding the sarcomere, corresponding to light SR. The Ca^{2+} leak and the Ca^{2+} transport occurred only at the SR layer.

Formulation of the functional equation system

The functional equation system in the present study was formed from the general Eq. 2 and the key term $F([Ca^{2+}], t)$, which governs all the binding reactions in the diffusion process. The kinetics of the binding of Ca^{2+} to a site (or buffer), B, is described as

$$[Ca^{2+}] + [B] \underset{k_{off}}{\overset{k_{on}}{\rightleftharpoons}} [CaB]. \tag{4}$$

This reaction can be expressed by the following ordinary differential equations and Eq. 2 for any nondiffusible binding site B:

$$\left.\begin{aligned} \frac{d[B]}{dt} &= k_{off,CaB}[CaB] - k_{on,CaB}[Ca^{2+}][B] \\ \frac{d[CaB]}{dt} &= k_{on,CaB}[Ca^{2+}][B] - k_{off,CaB}[CaB] \end{aligned}\right\}, \tag{5}$$

where $k_{on,CaB}$ and $k_{off,CaB}$ are forward and backward rate constants.

For a diffusible buffer such as D, a corresponding diffusion term must be added to the equations as

$$\left.\begin{aligned} \frac{\partial[D]}{\partial t} &= D_D\nabla^2[D] + k_{off,CaD}[CaD] \\ &\quad -k_{on,CaD}[Ca^{2+}][D] \\ \frac{\partial[CaD]}{\partial t} &= D_{CaD}\nabla^2[CaD] - k_{off,CaD}[CaD] \\ &\quad +k_{on,CaD}[Ca^{2+}][D] \end{aligned}\right\}, \tag{6}$$

where D_D and D_{CaD} are the diffusion coefficients for D and CaD, respectively.

For any nondiffusible binding sites we assume

$$[B]_T = [CaB] + [B] \tag{7}$$

at any time, where $[B]_T$ represents the total concentration of free- and Ca^{2+}-bound sites. However, for diffusible buffer, Eq. 7 is only valid at rest, i.e., before the simulation starts,

$$[B]_T = [CaB]_0 + [B]_0 \tag{8}$$

where subscript 0 indicates the initial time point 0. This is because, at rest, the diffusible buffers are assumed to be in steady state with Ca^{2+} and uniformly distributed so that there is no net diffusion of any buffer.

The first step in establishing each term in Eq. 3 was to identify all the Ca^{2+} binding sites (buffers) and diffusible species in the simulation. Three binding sites, troponin, parvalbumin, and Ca^{2+} pump were considered as nondiffusible in the present simulation. We assume that both D and CaD would diffuse in the cytoplasm and thus include the diffusion terms of D and CaD as well as that of Ca^{2+} in the equation system. Magnesium ions, Mg^{2+}, are involved in the binding reaction of Ca^{2+} with parvalbumin and may also be considered as diffusible species, although parvalbumin and magnesium-parvalbumin are considered nondiffusible because of the expected relatively slow diffusion of a protein compared to the time course of a Ca^{2+} spark. The forward reaction of Mg^{2+} and parvalbumin is very slow, so it was assumed that $d[MgPARV]/dt \approx 0$ at all times. In other words, $[MgPARV] = [MgPARV]_0 = \text{const}$. From this relation and Eq. 7 for nondiffusible parvalbumin,

$$\begin{aligned} [PARV]'_T &= [PARV]_T - [MgPARV]_0 \\ &= ([PARV] + [CaPARV] + [MgPARV]) \\ &\quad - [MgPARV]_0 \\ &= [PARV] + [CaPARV]. \end{aligned} \tag{9}$$

Also, because $\Delta[MgPARV] \ll [Mg^{2+}]$, we assumed $[Mg^{2+}] = [Mg^{2+}]_0 = \text{const}$. On the basis of this condition, we also assumed Mg^{2+} to be nondiffusible.

Starting from an equation system of a quantitative model of Ca^{2+} removal from the myoplasm described by Brum et al. (1988), and considering the above conditions, we formulated the following functional equation system for the diffusion and binding simulation:

General equations

$$\frac{\partial[Ca^{2+}]}{\partial t} = D_C\nabla^2[Ca^{2+}] - F([Ca^{2+}], t) \tag{10}$$

$$\begin{aligned} F([Ca^{2+}], t) &= \frac{d[CaTN]}{dt} + \frac{d[CaPARV]}{dt} + \frac{d[CaP]}{dt} \\ &\quad + \left(\frac{d[CaD]}{dt}\right)_F + V - L \end{aligned} \tag{11}$$

Binding equations

$$\begin{aligned} \frac{d[CaTN]}{dt} &= k_{on,CaTN}[Ca^{2+}]\{[TN]_T - [CaTN]\} \\ &\quad - k_{off,CaTN}[CaTN] \end{aligned} \tag{12}$$

$$\begin{aligned} \frac{d[CaPARV]}{dt} &= k_{on,CaPARV}[Ca^{2+}]\{[PARV]'_T \\ &\quad - [CaPARV]\} \\ &\quad - k_{off,CaPARV}[CaPARV] \end{aligned} \tag{13}$$

$$\begin{aligned} \frac{d[CaP]}{dt} &= k_{on,CaP}[Ca^{2+}]\{[P]_T - [CaP]\} \\ &\quad - k_{off,CaP}[CaP] - V \end{aligned} \tag{14}$$

$$\begin{aligned} \frac{\partial[D]}{\partial t} &= D_D\nabla^2[D] - k_{on,CaD}[Ca^{2+}][D] \\ &\quad + k_{off,CaD}[CaD] \end{aligned} \tag{15}$$

$$\frac{\partial[\mathrm{CaD}]}{\partial t} = D_{\mathrm{CaD}}\nabla^2[\mathrm{CaD}] + k_{\mathrm{on,CaD}}[\mathrm{Ca}^{2+}][\mathrm{D}] - k_{\mathrm{off,CaD}}[\mathrm{CaD}] \quad (16)$$

$$\left(\frac{\mathrm{d}[\mathrm{CaD}]}{\mathrm{d}t}\right)_{\mathrm{F}} = k_{\mathrm{on,CaD}}[\mathrm{Ca}^{2+}][\mathrm{D}] - k_{\mathrm{off,CaD}}[\mathrm{CaD}] \quad (17)$$

Pump transport and leak

$$V = k_{\mathrm{P}}[\mathrm{CaP}] \quad (18)$$

$$L = k_{\mathrm{P}}[\mathrm{CaP}]_0 \quad (19)$$

Site conservation equations

$$[\mathrm{TN}]_{\mathrm{T}} = [\mathrm{TN}] + [\mathrm{CaTN}] \quad (20)$$

$$[\mathrm{PARV}]_{\mathrm{T}} = [\mathrm{PARV}]'_{\mathrm{T}} + [\mathrm{MgPARV}]_0 \quad (21)$$

$$[\mathrm{PARV}]'_{\mathrm{T}} = [\mathrm{PARV}] + [\mathrm{CaPARV}] \quad (22)$$

$$[\mathrm{P}]_{\mathrm{T}} = [\mathrm{P}] + [\mathrm{CaP}] \quad (23)$$

$$[\mathrm{D}]_{\mathrm{T}} = [\mathrm{CaD}]_0 + [\mathrm{D}]_0 \quad (24)$$

$$[\mathrm{Mg}^{2+}]_{\mathrm{T}} = [\mathrm{MgPARV}]_0 + [\mathrm{Mg}^{2+}]_0 \quad (25)$$

Because CaD is a diffusible buffer, $(\mathrm{d}[\mathrm{CaD}]/\mathrm{d}t)_{\mathrm{F}}$ (Eq. 17) represents the nondiffusional terms (i.e., the Ca binding terms) in $\partial[\mathrm{CaD}]/\partial t$ for use in $F([\mathrm{Ca}^{2+}], t)$ in Eq. 11.

Eqs. 14, 18, and 19 correspond to the kinetic properties of a highly simplified 2-step model of the SR Ca^{2+} pump cycle presented in Scheme 1. In this model, the reversible binding of Ca^{2+} to a Ca^{2+}-free, cytosol-facing Ca^{2+} binding site (P) on the pump, with ON and OFF rate constants $k_{\mathrm{on,CaP}}$ and $k_{\mathrm{off,CaP}}$, is followed by a single irreversible step (rate constant k_{P}) that translocates the Ca^{2+} ion from the cytosol-facing pump binding site to the SR lumen and simultaneously regenerates a Ca^{2+}-free pump binding site facing the cytosol. V is the rate of Ca^{2+} translocation from the cytosol to the SR lumen, as well as the rate of regeneration of free pump sites by the pump transport cycle, and L is the rate of Ca^{2+} leak from the SR lumen to the cytosol. In this simplified scheme, the Ca^{2+} translocation step of the pump cycle eliminates one Ca^{2+}-occupied pump site (CaP) and regenerates a free pump site (P), but does not remove or release a free Ca^{2+} ion in the cytosol. Thus the rate of Ca^{2+} translocation by the pump must appear as a negative term ($-V$) in the expression for $\mathrm{d}[\mathrm{CaP}]/\mathrm{d}t$ (Eq. 14), but does not contribute to $F([\mathrm{Ca}^{2+}], t)$ and therefore must be removed (by adding V) when calculating the pump contribution to $F([\mathrm{Ca}^{2+}], t)$. This accounts for the presence of the term $+V$ in Eq. 11. Because, at rest, all the binding reactions are in equilibrium, the leak of Ca^{2+} from the SR was set equal to the transport of Ca^{2+} back to SR by the pump at rest. We further assumed that L was a constant throughout the simulations.

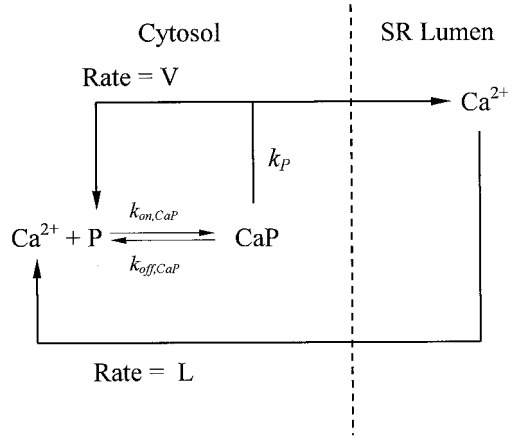

Scheme 1.

All the reaction rate constants and initial values in these equations are listed respectively in Tables 1 and 2. We used μM as the unit for the concentration and ms as the unit of time in all the simulations. For our starting calculations, the resting $[Ca^{2+}]$ was assumed to be 0.08 μM. The temperature of the simulations and experiments was 20°C.

The restriction of the diffusion process by SR membranes has been given special treatments. Kargacin (1994) used a barrier region with a diffusion coefficient of 10% of that in the rest of the cell to represent the superficial SR in smooth muscle whereas Pratusevich and Balke (1996) reduced the diffusion coefficient of the SR elements for Ca^{2+} to ⅕ of the value at other elements. A reducing factor, RF, of 0.5 was used arbitrarily with all the diffusion coefficients, D_{C}, D_{D} and D_{CaD}, at SR voxels in the present study.

Simulation of laser scanning confocal imaging

The fluo-3 fluorescence signal recorded experimentally from a muscle fiber is considered to be proportional to [CaD] (Klein et al., 1996). However, because of the limitation in the spatial resolution of LSCM, the spark images obtained under the conditions of experimental observation contain distortion and blurring of the actual distribution of [CaD] in the muscle. Therefore, no individual line or plane of the domain of distribution of [CaD] produced by the diffusion and binding simulation can be directly viewed as equivalent to the spark image recorded by the LSCM. The optical distortion and blurring of the LSCM system must also be simulated to produce simulated Ca^{2+} sparks comparable to the experimentally detected sparks. The way in which a microscope distorts and blurs an individual point in the specimen is described by its PSF.

A Gaussian kernel was used to approximate the microscopic PSF in the present simulation having spatial FWHM dimensions of 0.5 μm, 0.5 μm, and 1.0 μm, in length (x), depth (y), and height (z), respectively, corresponding to the approximate resolution of our confocal microscope. These values were selected to be slightly larger than those determined from examination of subresolution fluorescent beads in air on our confocal system (0.4 μm, 0.4 μm, 0.8 μm; Schneider and Klein, 1996). The slightly larger half-width values were used in the present simulations in an attempt to account for the likely greater optical distortion within a fiber.

The image of the simulated spark was generated as done from the experimental recordings (Klein et al., 1997) by first subtracting the value before the Ca^{2+} release, $[\mathrm{CaD}]_0$ or F_0, from the [CaD] or F values after the Ca^{2+} release starts, and then normalizing these $\Delta[\mathrm{CaD}]$ or ΔF differences to $[\mathrm{CaD}]_0$ or F_0 to give

$$\frac{F - F_0}{F_0} = \frac{[\mathrm{CaD}] - [\mathrm{CaD}]_0}{[\mathrm{CaD}]_0}. \quad (26)$$

NUMERICAL METHODS AND COMPUTER PROGRAMMING

Numerical methods for the simulation of diffusion and binding

In the present simulation, the finite difference method was chosen as the numerical method for the solution of the partial differential equations. However, the explicit implementation of the finite difference method is only conditionally stable. In the present study, the stability criterion of the explicit method was satisfied by reducing the time step used in the simulation. The explicit Euler method (Atkinson, 1989) was used to solve the ordinary differential equations in the equation system, Eqs. 10–25. The complete set of finite difference equations for Eqs. 10–19 is listed in Appendix A.

TABLE 1 Starting values of the rate constants for binding sites

Definition	Symbol	Value	Source
Troponin with Ca^{2+}			
Forward	$k_{on,CaTN}$	0.12 $\mu M^{-1}ms^{-1}$	Cannell and Allen, 1984
Backward	$k_{off,CaTN}$	0.12 ms^{-1}	Cannell and Allen, 1984
Dissociation	K_D	1.0 μM	
Pump with Ca^{2+}			
Forward	$k_{on,CaP}$	0.4 $\mu M^{-1}ms^{-1}$	Inesi and de Meis, 1989
Backward	$k_{off,CaP}$	0.4 ms^{-1}	Assumed
Dissociation	K_D	1.0 μM	Assumed
Translocation	k_P	4.0×10^{-4} ms^{-1}	Assumed
Dye (fluo-3) with Ca^{2+}			
Forward	$k_{on,CaD}$	0.236 $\mu M^{-1}ms^{-1}$	Escobar et al., 1997
Backward	$k_{off,CaD}$	0.175 ms^{-1}	Escobar et al., 1997
Dissociation	K_D	0.74 μM	
Parvalbumin			
Parvalbumin with Ca^{2+}			
Forward	$k_{on,CaPARV}$	0.25 $\mu M^{-1}ms^{-1}$	Cannell and Allen, 1984
Backward	$k_{off,CaPARV}$	1.0×10^{-3} ms^{-1}	Cannell and Allen, 1984
Dissociation	K_D	4.0×10^{-3} μM	
Parvalbumin with Mg^{2+}			
Forward	$k_{on,MgPARV}$	6.6×10^{-5} $\mu M^{-1}ms^{-1}$	Cannell and Allen, 1984
Backward	$k_{off,MgPARV}$	6.0×10^{-3} ms^{-1}	Cannell and Allen, 1984
Dissociation	K_D	90.9 μM	
ATP*			
ATP with Ca^{2+}			
Forward	$k_{on,CaATP}$	0.15 $\mu M^{-1}ms^{-1}$	Baylor and Hollingworth, 1998
Backward	$k_{off,CaATP}$	30.0 ms^{-1}	Baylor and Hollingworth, 1998
Dissociation	K_D	200.0 μM	
ATP with Mg^{2+}			
Forward	$k_{on,MgATP}$	1.5×10^{-3} $\mu M^{-1}ms^{-1}$	Baylor and Hollingworth, 1998
Backward	$k_{off,MgATP}$	0.15 ms^{-1}	Baylor and Hollingworth, 1998
Dissociation	K_D	100.0 μM	

*Ca^{2+} binding to ATP was not included in the starting model.

The first step of the implementation of the finite difference method in the present simulation was the discretization of the computational domain. In this study, we adopted the definition that a voxel is the discrete volume element of the continuous specimen and the 3D equivalent of a pixel, which is the basic element of a 2D image (Pawley, 1995). Therefore the terms voxel, pixel, and grid point are often used interchangeably in the text. We discretized the computational domain into even-sided cubic voxels much smaller than the image pixels of the confocal microscope (Fig. 1, *B–D*). Using even-sided cubic voxels ensures the same accuracy of the finite differentiation in all three dimensions. A finer network near the Ca^{2+} source is necessary to ensure adequate computing accuracy of diffusion near the source, whereas a coarser network far away from the calcium source is more computationally efficient in significantly reducing the computing time of the simulation and required storage space of the results. Therefore, the entire computational domain was divided into a total of four network blocks, one fine network block (F) and three coarse network blocks (A, B, and C). A schematic diagram of the 3D view of the whole computational domain with the arrangement of the four blocks is shown in Fig. 1 *B*. The Ca^{2+} spark is considered to originate from a point source located at the origin of this coordinate system. The spatial distance between the neighboring points of the coarse network was set as two times that of the fine network, so that the points of the coarse networks at the interface coincide with half of the points of the fine network at the interface. Figure 1, *C* and *D* show the two side views of the computational domain. The simulation results within the three coarse blocks were linearly interpolated to match the spacing of the fine grid.

The main mathematical operation involved with the simulation of LSCI is the 3D discrete convolution of the spatial-temporal distribution of [CaD], as obtained from the solution of the diffusion and binding simulation, with the Gaussian kernel for the confocal microscope.

The code for the diffusion and binding simulation was written in FORTRAN 77 language under IRIX 6.2 on an SGI workstation (Mountain View, CA). Double precision variables were used in the computation to reduce rounding errors. All code was optimized manually as well as by setting the appropriate options for the FORTRAN compiler for efficient parallel processing. Diffusion and binding simulations were performed on a Power Challenge 10000 XL Series of SiliconGraphics Computer System, which has twenty 194-MHz IP25 processors.

In experimental recording of Ca^{2+} sparks, the line-scan fluorescence image is constructed by repeatedly scanning the same line along the fiber at 2-ms intervals (Schneider and Klein, 1996). The diffusion and binding simulation results were output at 1-ms intervals, for a total of 30 ms, which produces a higher temporal resolution in the simulated images of LSCM than that in the experimentally recorded images.

All the simulation outputs were saved as single precision data in binary file to reduce disk storage space. In addition, a text log file containing all the parameters used in the current simulation was produced at the beginning of each simulation for the reference of the analysis of the results.

Algorithm development for LSCI simulation

All the results from the diffusion and binding simulation need to be further processed for visualization and analysis. A program written in MATLAB5 was used to carry out the 3D discrete convolution for the simulation of the LSCI in this study. Because the main simulated scan line coincides with the long axis of the computational domain passing through the Ca^{2+} release source (the x axis of the coordinate system in Fig. 1 *B*), the consolidated domain was extended (flipped from the positive axis directions) to the $-x$, $-y$, and $-z$ directions to such an extent that there would be enough points

TABLE 2 Starting values of the parameters used in the simulation

Definition	Symbol	Value	Source
Differential coefficient of Ca^{2+}	D_C	0.7 $\mu m^2 ms^{-1}$	Cannell and Allen, 1984
Differential coefficient of D	D_D	0.09 $\mu m^2 ms^{-1}$	Harkins et al., 1993
Differential coefficient of CaD	D_{CaD}	0.09 $\mu m^2 ms^{-1}$	Assumed to be equal to D_D
Differential coefficient of ATP*	D_{ATP}	0.14 $\mu m^2 ms^{-1}$	Baylor and Hollingworth, 1998
Differential coefficient of CaATP*	D_{CaATP}	0.14 $\mu m^2 ms^{-1}$	Baylor and Hollingworth, 1998
Differential coefficient of MgATP*	D_{MgATP}	0.14 $\mu m^2 ms^{-1}$	Baylor and Hollingworth, 1998
Diffusion reducing factor	RF	0.5	
Magnitude of Ca^{2+} current	I	1.4 pA	Pratusevich and Balke, 1996
Geometrical parameters			
Sarcomere length		4.0 μm	Klein et al., 1991
Sarcomere width		1.0 μm	Alberts et al., 1989
Troponin length		2.0 μm	Aidley, 1978
Temporal parameters			
Ca^{2+} release time		8.0 ms	
Simulation time		30.0 ms	
Total and initial concentrations			
Total troponin	$[TN]_T$	240.0 μM	Baylor et al., 1983
Total parvalbumin	$[PARV]_T$	1000.0 μM	Baylor et al., 1983
Total ATP	$[ATP]_T$	5000.0 μM	Lab data
Total pump	$[P]_T$	200.0 μM	Baylor et al., 1983
Total dye	$[D]_T$	50.0 μM	Schneider and Klein, 1996
Resting Ca^{2+}	$[Ca^{2+}]_0$	0.08 μM	Klein et al., 1996
Resting magnesium	$[Mg^{2+}]_0$	1000.0 μM = const.	

*Ca^{2+} binding to ATP was not included in the starting model.

around the x axis when the 3D discrete convolution of those points with the Gaussian kernel was performed along the x axis. Finally, the 3D discrete convolution was performed on this consolidated and extended domain at specified locations to produce the simulated sparks viewed from different positions and defocuses relative to the Ca^{2+} releasing point. Because of the symmetries in the simulation domain, any simulated spark produced in the computational domain is just half of the entire spark in the positive x direction. Each spark image was converted to a ratio image using Eq. 26 and "flipped" to the other half of the simulation domain in the negative x direction to form a complete spark.

Initialization of the simulation

We assumed that, at the far-end boundaries of the computational domain,

$$\left.\begin{aligned}[Ca^{2+}](t, x, y, h) &= [Ca^{2+}]_0\\ [Ca^{2+}](t, x, d, z) &= [Ca^{2+}]_0\\ [Ca^{2+}](t, l, y, z) &= [Ca^{2+}]_0\end{aligned}\right\} \quad (t \geq 0), \tag{27}$$

where h, d, and l are the height, depth, and length of the computational domain respectively (Fig. 1 *B*), and $[Ca^{2+}]_0$ is the resting value of the $[Ca^{2+}]$. Because the three near-end boundaries of the computational domain are the symmetrical planes of the simulation domain, no crossing flux exists. Therefore, the near-end boundary conditions are (Fig. 1 *B*)

$$\left.\begin{aligned}\frac{\partial[Ca^{2+}](t, 0, y, z)}{\partial x} &= 0\\ \frac{\partial[Ca^{2+}](t, x, 0, z)}{\partial y} &= 0\\ \frac{\partial[Ca^{2+}](t, x, y, 0)}{\partial z} &= 0\end{aligned}\right\} \quad (t \geq 0). \tag{28}$$

The boundary conditions for D and CaD were treated by equations analogous to Eqs. 27 and 28 for Ca^{2+}.

Before the start of the simulation, $[Ca^{2+}]$ and [D] were assumed to be uniformly distributed in the sarcomere, and all Ca^{2+} binding sites and buffers were assumed to be at their equilibrium levels corresponding to a resting $[Ca^{2+}]_0$ of 80 nM (Klein et al., 1996). We use $[CaTN]_0$, $[CaPARV]_0$, $[MgPARV]_0$, $[CaP]_0$, and $[CaD]_0$ to denote the initial values of the concentration of the Ca^{2+} binding sites and buffers. Note that, even though spatial point indices have been ignored, the total concentration of troponin ($[TN]_T$) and SR Ca^{2+} pump sites ($[P]_T$) are different in different spatial locations, so the $[CaTN]_0$ and $[CaP]_0$ will also vary with locations. The expressions for the initial values of all the reactants are given below.

$$[Ca^{2+}]_0 = 0.08\ \mu M \tag{29}$$

$$[CaTN]_0 = \frac{k_{on,CaTN}[Ca^{2+}]_0[TN]_T}{k_{on,CaTN}[Ca^{2+}]_0 + k_{off,CaTN}} \tag{30}$$

$$[CaPARV]_0 = (A/G)[PARV]_T \tag{31}$$

$$[MgPARV]_0 = (B/G)[PARV]_T \tag{32}$$

$$[CaP]_0 = \frac{k_{on,CaP}[Ca^{2+}]_0[P]_T}{k_{on,CaP}[Ca^{2+}]_0 + k_{off,CaP} + k_P} \tag{33}$$

$$[CaD]_0 = \frac{k_{on,CaD}[Ca^{2+}]_0[D]_T}{k_{on,CaD}[Ca^{2+}]_0 + k_{off,CaD}} \tag{34}$$

$$V_0 = k_P[CaP]_0 \tag{35}$$

$$L = V_0 \tag{36}$$

$$[TN]_0 = [TN]_T - [CaTN]_0 \tag{37}$$

$$[PARV]_0 = [PARV]_T - [CaPARV]_0 - [MgPARV]_0 \tag{38}$$

$$[P]_0 = [P]_T - [CaP]_0 \tag{39}$$

$$[D]_0 = [D]_T - [CaD]_0 \tag{40}$$

where

$$A = \frac{k_{on,CaPARV}}{k_{off,CaPARV}}[Ca^{2+}]_0$$

$$B = \frac{k_{on,MgPARV}}{k_{off,MgPARV}}[Mg^{2+}]_0$$

$$G = 1 + A + B.$$

All diffusion and binding simulations started with a release of Ca^{2+} from a source at the origin. The rate, R_r, at which free $[Ca^{2+}]$ would increase in the origin voxel due to this release in the absence of diffusion and binding was given by

$$R_r = \frac{d[Ca^{2+}]_{source}}{dt} = \frac{I}{\mathcal{F}zv}, \quad (41)$$

where I is the Ca^{2+} current, $\mathcal{F}$ is the Faraday constant, z is the valence of Ca^{2+} and v is the volume of the voxel of Ca^{2+} release. For our "starting" simulation, I is a square pulse with a magnitude of 1.4 pA (Pratusevich and Balke, 1996), $\mathcal{F} = 9.65 \times 10^4$ Cmol^{-1}, $z = 2$, and $v = 0.0333^3 = 3.6926 \times 10^{-5}$ μm^3,

$$R_r = 1.96 \times 10^5 \ \mu M \ ms^{-1}. \quad (42)$$

The start of this constant Ca^{2+} release was set at 1 ms after the start of the simulation, so that the first simulation output file at the end of the first millisecond contained the resting value under the simulation without release. This resting value was used in Eq. 26. The Ca^{2+} release time was chosen as a fixed 8.0 ms (Table 2) to match the mean rise-time (10–90%) of experimentally measured sparks (Klein et al., 1997). The total simulation time of 30.0 ms (Table 2) is long enough because sparks from experimental recordings have been identified with a 3.3-μm $\times$ 20-ms box (Klein et al., 1997).

Program testing

The FORTRAN programs for the diffusion and binding simulation were tested in several limiting cases. The computational and kinetic stabilities were tested under the condition of no Ca^{2+} release for the entire simulation period. After 1.35×10^5 time increments at 2.2×10^{-4} ms per increment, with repeated computations at each of over 60,000 grid points for each time increment, the MPE in $[Ca^{2+}]$, [D], or [CaD] among almost 400,000 grid points in the consolidated computational domain was less than 0.38%, demonstrating stability of the model in the absence of Ca^{2+} release. Similar results were obtained when simulation was performed with $D_C = D_D = D_{CaD} = 0.0$ and $[Ca^{2+}] = 100$ μM at the release source, indicating that the diffusion coefficients were properly coded in the program. Another important test was to compare the numerical and analytical solutions for the case of diffusion from both an instantaneous and a continuous point source of Ca^{2+} under the condition of no binding reactions. The numerical simulation of pure diffusion was generated by setting all the kinetic rate constants and the initial $[Ca^{2+}]$, [D] and [CaD] to zero except the $[Ca^{2+}]$ at the origin and setting the reducing factor of the diffusion coefficients to 1.0 before the start of the simulations. The error in the numerical solution compared to the analytical solution was estimated by examining the MPE and the MSPE or the RMSPE. The MPE between the numerical and analytical solutions for diffusion along a specified line is the maximum of all the percentage errors at all points along the line. The percentage error at any point was calculated relative to the peak of the corresponding analytical solution along a line on which that point resides. The MSPE or RMSPE was used to describe quantitatively the general agreement of the numerical and analytical solutions. The MSPE for a comparable line was calculated by summing the squares of the percentage errors at all the points on the line and dividing by the total number of the points on the line. For the case of pure diffusion from an instantaneous point source, the starting $[Ca^{2+}]$ at the origin was set to 100 mM and then allowed to diffuse throughout the surrounding medium. The numerical and analytical solutions were compared at 0.133 ms after the diffusion started, before the diffusion reached the nearest boundary of the computational domain. The MPE for the comparisons along x, y, and z axes of the computational domain were 0.26, 1.14, and 0.26%, respectively. The MSPE (RMSPE) for these comparisons were 0.02 (0.13), 0.24 (0.49), and 0.01 (0.12), respectively. Pure diffusion from a continuous point source of constant Ca^{2+} release rate, corresponding to a 1.4 pA Ca^{2+} current as in the spark simulation, was used to generate both numerical and analytical solutions. Because the analytical solution used in this comparison represented a continuous point source at a constant release rate, we set the Ca^{2+} efflux time to the entire calculation period instead of only a fraction of the entire calculation period as in spark simulations, to obtain a pseudosteady-state distribution of Ca^{2+} for comparison with the analytical solution for diffusion from a point source (Crank, 1975). Two comparisons were made on the numerical and analytical solutions of the diffusion from a continuous source. One was the comparison of the numerical and analytical time courses of the $[Ca^{2+}]$ at a point about 0.2 μm from the source, and the other a comparison of the numerical and analytical spatial spreads of $[Ca^{2+}]$ along three coordinate axes at the end of 0.5 ms. For the time course of about 3.0-ms duration the MPE was 1.42% and the MSPE (RMSPE) was 0.52 (0.72). For the spatial spread comparisons in x, y, and z directions, the MPE and MSPE (RMSPE) were 0.83%, 0.03 (0.17); 0.75%, 0.14 (0.37); and 0.84%, 0.03 (0.16), respectively. These comparison results indicated that the implementation of the numerical method in the FORTRAN programs was satisfactory.

RESULTS

Selection of starting values of model parameters

The simulation of Ca^{2+} sparks began with the parameter values listed in Tables 1 and 2, which serve as the "starting" parameter values for our simulation. These values were selected to agree with parameter values used in various earlier simulations of average or local changes in free and bound Ca^{2+} during Ca^{2+} release in muscle fibers. Our choice of these starting values represents a somewhat arbitrary starting point in parameter space, from which we can explore the effects of changing various values on the simulated sparks.

Adjustments were made to the values of $[TN]_T$ and $[P]_T$ given in Table 2 based on the nonuniform distribution of troponin and the SR Ca^{2+} pump within the sarcomere. $[TN]_T = 240$ μM is the average concentration of troponin C Ca^{2+}-specific binding sites over the entire fiber volume. Since troponin C is located only in the I band, which constitutes only half of the sarcomere when stretched to 4 μm per sarcomere, we doubled the troponin concentration to $[TN]_{T,I} = 480$ μM for the total troponin concentration in the I band region of the sarcomere in our simulation within a 1-μm longitudinal distance from the Z line and set it to zero in the remainder of the sarcomere. The Ca^{2+} pump was considered as being distributed only on the surface of the myofibril where the SR is located instead of distributed uniformly throughout the whole volume of the sarcomere. Therefore, an adjustment was made to compensate for the difference between the $[P]_T$ on the surface of sarcomere and that averaged over the entire volume of the sarcomere. In our fine-mesh network, the number of voxels on the surface of the myofibril is ⅛ the number of voxels in the volume of

the myofibril. The $[P]_T$ value on the surface, $[P]_{T,S}$, was thus assumed to be eight times of that of the average concentration over the entire volume (200 μM), and therefore, a value of $[P]_{T,S} = 1600$ μM was used in the surface voxels in the fine mesh region in the starting simulation.

Spark simulation using starting parameter values

The characteristics of Ca^{2+} sparks are usually described by the peak amplitude of the spark, the rise time (here defined as the time to go from 10 to 90% of peak amplitude), the temporal FDHM and the spatial FWHM. We therefore examined the simulated Ca^{2+} sparks by plotting the values along two orthogonal lines passing through the location of the peak of the spark, giving the time course and the spatial spread of the simulated spark as shown in Fig. 2, *A* and *B*, respectively. This spark was simulated with the parameters from Tables 1 and 2 for a 1.4-pA point source of Ca^{2+} release located in the terminal SR and active for 8 ms. The spark time course at the center of the simulated spark (Fig. 2 *A*) rises monotonically throughout the 8-ms period of simulated Ca^{2+} release, and then abruptly begins to decline at the cessation of Ca^{2+} release. The spatial profile (Fig. 2 *B*) at the time of the peak of the simulated spark exhibits a bell-shaped distribution. The Peak amplitude of the simulated spark is 1.12 in the dimensionless units of $\Delta[CaD]/[CaD]_0$, which correspond to the dimensionless units of $\Delta F/F_0$ of experimentally recorded Ca^{2+} sparks, and its rise time, FDHM and FWHM were 6.1 ms, 7.7 ms, and 1.0 μm, respectively. Because the simulated spark (Fig. 2, *A* and *B*) was generated from a conservative set of parameters (Tables 1 and 2), it was considered as our starting spark for comparison with sparks simulated using other alternative sets of parameters (below).

Comparison with experimentally recorded sparks

An important issue concerning the Ca^{2+} sparks simulated with any model is the extent to which the simulated sparks agree or disagree with experimentally observed sparks. Ultimately, the goal of modelling a Ca^{2+} spark is to reproduce as closely as possible any experimentally recorded Ca^{2+} spark. This long-range goal is, however, beyond the scope of the present paper, which primarily introduces our present model and examines how the values of various parameters in the model influence the simulated sparks. None the less, it is still important that the results of our present simulations exhibit characteristics that are generally consistent with the average properties of experimentally observed Ca^{2+} sparks.

Figure 2, *C* and *D* present the time course and spatial distribution at time of peak obtained by spatiotemporally superimposing and averaging six individual experimentally recorded Ca^{2+} sparks in a train of repetitive mode sparks (Klein et al., 1999). Repetitive mode events were selected for this display because they arise at a single triad, apparently from the repetitive opening of either the same group of Ca^{2+} release channels or of the same single channel (Klein et al., 1999). These repetitive events are thus not influenced by the effects of variations in the distance of the scan line from the release channels (below). The spark simulated with the starting parameter values (Fig. 2 *A*) has only about half the amplitude of the experimental spark in Fig. 2 *C*, indicating that the release current magnitude may be too low to account for this experimental record (see below), but the rise time (6.1 ms) and FDHM (7.7 ms) of the simulated spark are roughly similar to those of the experimental record (4.7 and 8.4 ms, respectively). The spatial distribution (Fig. 2 *B*) of the spark simulated with the starting parameter values is considerably more narrow (FWHM 1.0 μm) than that of the experimental spark (Fig. 2 *D*; FWHM 2.2 μm). A more extensive comparison of the properties of simulated and experimentally measured sparks will be presented in the Discussion.

Effects of the confocal imaging system

The time courses and lateral distributions of both the theoretical (Fig. 2, *A* and *B*) and experimentally observed (Fig. 2, *C* and *D*) confocal fluorescence signals were each calculated or recorded with finite optical and spatial resolution through the confocal microscope system. The theoretical records were obtained by first calculating the actual value of $\Delta[CaD]/[CaD]_0$ for each voxel in the solution space and then simulating the confocal line-scan image of this calculated spatial distribution (see Methods). In this case, it is thus possible to directly compare the theoretical confocal records with the underlying calculated change occurring within any individual voxel. Figure 2 *E* presents a comparison of the normalized theoretical time courses calculated within the origin voxel into which SR Ca^{2+} release occurs, with the theoretical time course for a confocal recording centered at the same voxel. In contrast to the rather smoothly declining rate of rise and fall of the simulated confocal time course (*points*), the local time course within the origin voxel (*line*) exhibits a more biphasic rise and fall, attaining more than 70% of its final level within the first millisecond and then gradually approaching its final level. This difference arises from the finite spatial resolution of the confocal system, which samples a range of voxels within the Gaussian kernel of the origin voxel, representing the spatial range of sampling in confocal recording. Such extended spatial sampling tends to smooth out the abrupt rise and fall of fluorescence calculated for the origin voxel itself. As a result of the much broader sampling of the confocal simulation compared to the individual origin voxel, the actual peak changes in the theoretical $\Delta[CaD]/[CaD]_0$ signals were 4.88 for the origin voxel in Fig. 2 *E*, but only 1.12 after simulation of confocal line-scan imaging (cf. Fig. 2 *A*).

The calculated spatial distribution of normalized fluorescence in a linear array of individual voxels parallel to the

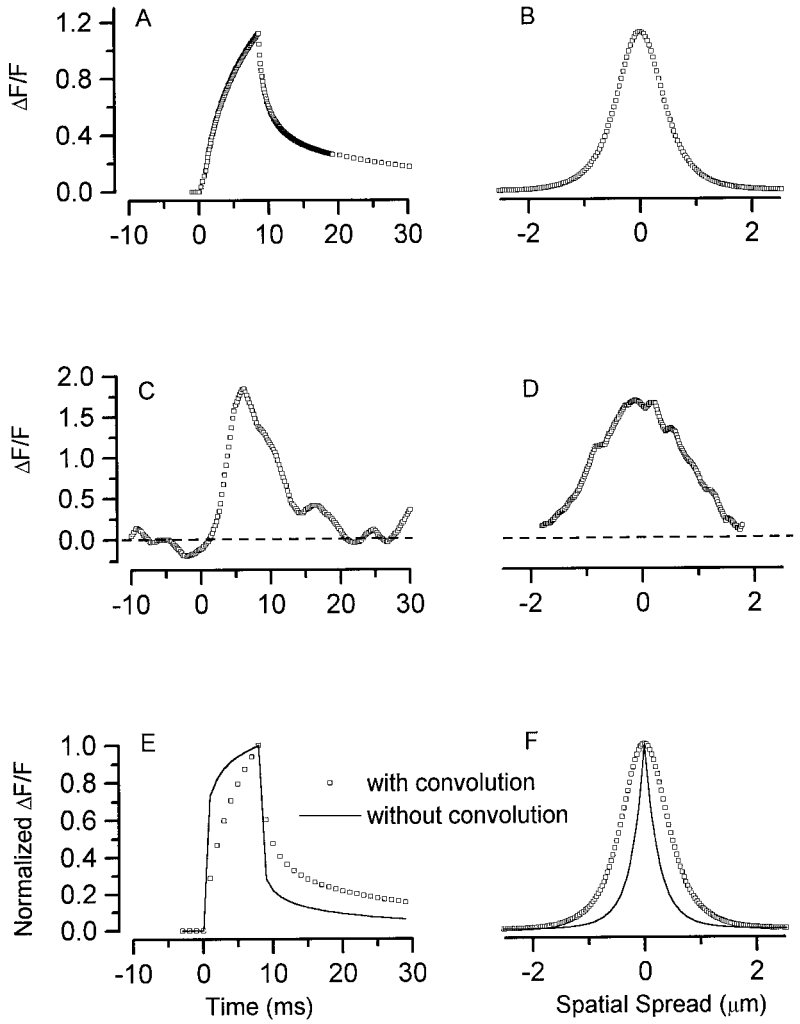

FIGURE 2 Ca^{2+} sparks simulated using the starting set of parameter values in the sarcomeric diffusion and binding model. (*A*) Time course of the peak of the simulated Ca^{2+} spark. In most cases this time course was used to characterize Ca^{2+} sparks simulated with different parameters. (*B*) Spatial spread passing through the peak of the simulated starting spark. This simulated spark was considered to be the starting spark, and the parameters (Tables 1 and 2) used in its simulation were defined as our starting parameters. (*C*) and (*D*) Time course and spatial spread of experimentally observed spark. These records are the average of six spontaneously activated repetitive events arising at the same location (Klein et al., 1999). (*E*) and (*F*) Comparisons of normalized, with corresponding peaks of each line, time courses, and spatial spreads of the simulated $\Delta[CaD]/[CaD]_0$ before (——) and after (□) its convolution with the Gaussian kernel. The peak values of $\Delta[CaD]/[CaD]_0$ were 4.88 before convolution and 1.12 after convolution.

fiber axis and passing through the origin voxel (Fig. 2 *F*, *line*) exhibits a much sharper spatial falloff away from the origin than in the simulated confocal recording of spatial distribution of normalized signal along the same scan line for the same solution of the diffusion and binding model. The broader spatial distribution of fluorescence change in the confocal simulation compared to that in the line of individual voxels is related to simulation of the confocal image from sampling a number of voxels within the Gaussian volume of the point of recording, rather than sampling an individual voxel. Nonetheless, the lateral distribution of fluorescence in the actual experimental recording (Fig. 2 *D*) is still considerably broader than the confocal simulation of the theoretical model (Fig. 2 *B*). The FWHM of the Gaussian kernel used for these simulations was slightly larger than the experimentally measured lateral FWHM of the microscope PSF for subresolution fluorescent beads in air. Thus, the fact that the experimentally observed spatial distribution of a spark was considerably wider than the spatial spread simulated for confocal recording could be due to either an underestimate of the distortion introduced by the confocal system or to failure of the present release, diffusion, and binding model to perfectly reproduce the actual spatiotemporal distribution of [CaD] within the fiber.

Effect of scan line position

A natural question about the experimentally observed sparks concerns the relationship between the position of the scan line relative to the Ca^{2+} source underlying the observed spark and the characteristics, (i.e., Peak, rise time, FDHM, and FWHM), of the observed sparks. To investigate the properties of sparks recorded from different positions relative to the site of origin, five scan lines in addition to the one passing through the origin (Fig. 2) were selected as shown in Fig. 3. The arrangement of these lines was similar to that used in similar simulations by Pratusevich and Balke (1996), but with lateral displacement (shift in y) and defocus distances (shift in z) appropriate to the approximate resolution of the confocal system used in measurements of Ca^{2+} sparks in our laboratory. Lines 2 and 3 are along the same optical axis as line 1 but defocused by 0.5 μm and 1.0 μm, respectively, from the point of Ca^{2+} release. These two

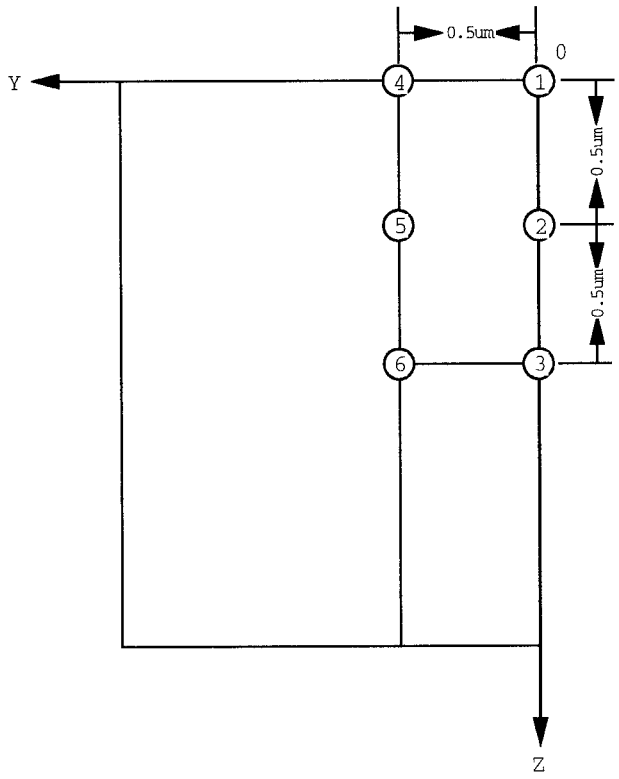

FIGURE 3 Positions of the six simulated scan lines. *Line 1*, corresponds to the confocal line scan through the location of the Ca^{2+} release site. *Line 2* and *line 3* are two lines with the same optical axis of *line 1*, but defocused by 0.5 μm and 1.0 μm from the release site, respectively. *Lines 4*, *5*, and *6* are along the same optical axis, but 0.5 μm away from the optical axis of *line 1*. *Line 5* and *line 2* are on the same focal plane, and so are the *line 6* and *line 3*.

lines will provide information about the effect of defocus on the observed sparks. Lines 4, 5, and 6 are along a different optical axis, which is displaced laterally by 0.5 μm from the optical axis of line 1. Lines 5 and 2 are on the same focal plane as are lines 6 and 3.

The time courses and spatial spreads of sparks scanned at these six lines for the distribution of [CaD] simulated using the starting parameters are shown in Fig. 4, *A* and *B*, respectively. Figure 4 *C* shows the normalized time courses, whereas the normalized spatial spreads are shown in Fig. 4 *D*. From both Fig. 4, *A* and *B*, it is clear that both defocus and lateral displacement of the scan line have a significant influence on the amplitude (peak) of the sparks as found previously by Pratusevich and Balke (1996) in their simulation of cardiac Ca^{2+} sparks. If the amplitude cut-off criterion for spark selection is 0.45 (Shirokova et al., 1997) or 0.5 (Klein et al., 1997), then only the [Ca^{2+}] transients generated with the starting parameter values and viewed at lines 1, 2, and 4 would be identified as sparks. The others, viewed at lines 3, 5, 6, and farther away, would not be identified as sparks. The peak of line 4 is less than half of that of line 1 and just around 0.45, so it might not be selected as a spark. In contrast, the magnitudes of lines 1 and 2 are well above the cut-off criteria. From these results, it is clear that the sparks identified from experimental recordings would be [Ca^{2+}] transients scanned within a lateral (*Y*) displacement of a half myofibril (0.5 μm) away from the Ca^{2+} release source or scanned at a defocus (*Z*) of less than one myofibril from the Ca^{2+} release source if our starting simulation parameter values are valid. Because only the [Ca^{2+}] transients scanned at lines 1 and 2 could be considered to be sparks and because the Ca^{2+} sparks scanned at these locations were fairly similar in magnitude, only the sparks scanned at line 1 were examined in the following simulations to determine properties of sparks using various changes in parameter values.

Figure 4 *C* indicates that the rise times of the time courses at all six scan lines are very similar and thus independent of their respective amplitudes. The 10–90% rise times for these records were 5.8, 5.8, 5.6, 5.6, 5.5, and 5.2 ms, respectively, for lines 1–6. In other words, the rise time of a simulated spark is minimally affected by the position of the scan line. This is consistent with the experimental observation of spark rise time being independent of spark amplitude (Klein et al., 1997). Indeed, our simulations indicated that the rise time is mainly determined by the duration of the Ca^{2+} release underlying the Ca^{2+} spark. From Fig. 4, *C* and *D*, it is obvious that the shapes of the spatial spread from the spark scanned at these six positions are very similar, and the shapes of the time courses for these positions are also quite similar, with a tendency to become more flat in the decay phase when the scan line is moved farther away from the Ca^{2+} releasing source. These conclusions regarding the effect of spark location on event time course are generally similar to those of Pratusevich and Balke (1996).

Effect of magnitude of Ca^{2+} release current

The rate of efflux of Ca^{2+} ions from the SR Ca^{2+} channels that generate the spark is a model parameter value that has major impact on the amplitude of the simulated Ca^{2+} spark. Doubling the assumed Ca^{2+} current into the origin voxel, from the value of 1.4 pA used in the starting simulation to a value of 2.8 pA, increased the peak $\Delta F/F$ almost proportionately (Fig. 5 *A*). The peak $\Delta F/F$ increased from 1.12 in the starting simulation to 2.21 when the release current was doubled. Doubling the release current caused an increase of $\Delta F/F$ at all locations along the scan line (Fig. 5 *B*). The amplitude of the simulated change in fluorescence was increased by essentially the same factor at all times and at all spatial locations, as indicated by the near identity of the normalized time course of $\Delta F/F$ at the origin (Fig. 5 *C*) and of normalized spatial distribution of $\Delta F/F$ (Fig. 5 *D*) for the simulations using 1.4 and 2.8 pA for the Ca^{2+} release current. These simulations thus indicate that the observed fluorescence amplitude at any location was essentially proportional to the assumed Ca^{2+} efflux rate, at least for assumed flux rates within a factor of 2 from the starting value, and that the relative time course and relative spatial

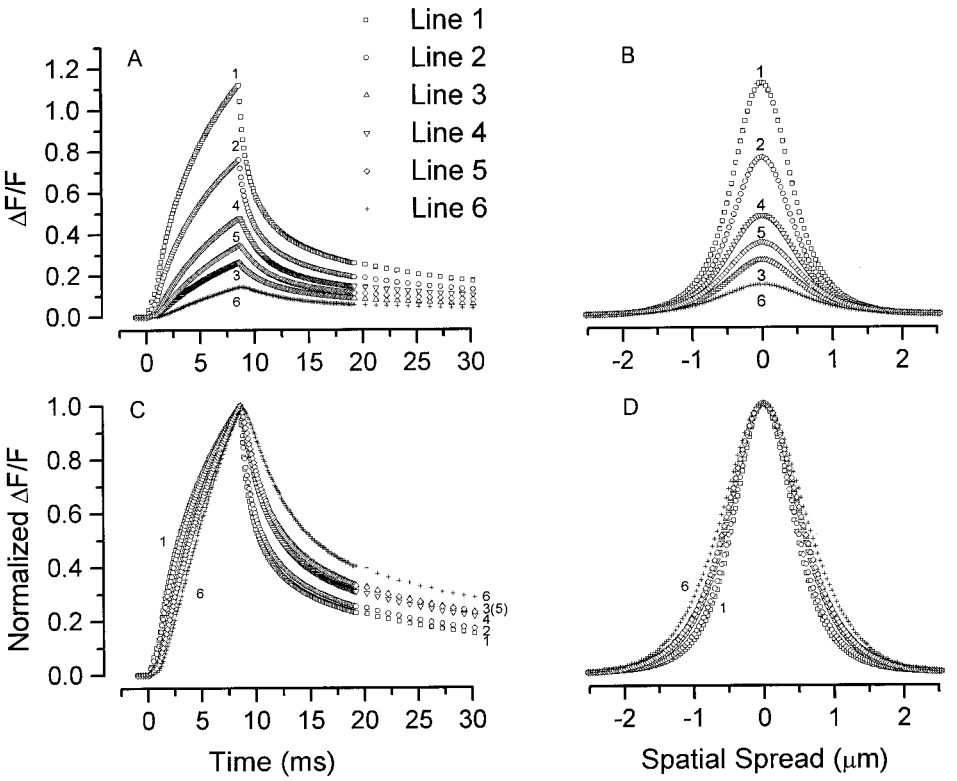

FIGURE 4 (*A*) Comparison of the time courses of the starting sparks scanned at six different positions as shown in Fig. 3. From this graph, it can be seen that the peaks of *line 1* and *line 2* are well above the selection criterion of sparks in experimental recordings (Klein et al., 1997), whereas those of *lines 3–6* are smaller than the selection criterion. (*B*) Comparison of the spatial spreads of the starting sparks scanned at six different positions as shown in Fig. 3. (*C*) and (*D*) are (*A*) and (*B*) normalized with respect to the corresponding peaks of each lines.

distribution of fluorescence in the simulated sparks were insensitive to the assumed magnitude of the release current.

Effect of Ca^{2+} diffusion coefficient

Diffusion of Ca^{2+} ions away form the point of Ca^{2+} release is expected to be the major mechanism for dispersion of the released Ca^{2+} ions. In the starting simulation, the diffusion coefficient for Ca^{2+} was set equal to the value of the Ca^{2+} diffusion coefficient in free solution. However, the diffusion coefficients of many molecules along a muscle fiber have been found to be lower than the values in free solution by a factor of about 2 (Kushmerick and Podolsky, 1969), presumably due to tortuosity or obstruction along the diffusion path. The effective diffusion constant for Ca^{2+} was much lower than for other ions or molecules (Kushmerick and Podolsky, 1969), presumably reflecting the effects of the myoplasmic Ca^{2+} binding and transport processes, which are already explicitly included in the present model. To examine the effects of possible lower rates of diffusive movement of Ca^{2+} in muscle fibers, we carried out simulations in which D_C was set at ½ the starting value. The change in D_C caused a 29% increase in the peak value of simulated $\Delta F/F$ (Fig. 6 *A*). Despite the increase in peak $\Delta F/F$, halving the diffusion constant for Ca^{2+} resulted in only minor changes in the time course of normalized $\Delta F/F$ at the origin (Fig. 6 *C*) and in negligible change in the spatial distribution of normalized $\Delta F/F$ (Fig. 6 *D*). Thus, although the amplitude of the simulated fluorescence in a spark was increased somewhat by halving the Ca^{2+} diffusion coefficient, the relative spatial spread and time course of the simulated spark were basically unaffected.

Effect of transport rate by the SR Ca^{2+} pump

In contrast to Ca^{2+} diffusion, which is one of the most immediate mechanisms for dispersion of Ca^{2+} from the vicinity of the Ca^{2+} release channels generating a spark, the translocation step of the SR Ca^{2+} pump is one of the slowest components of Ca^{2+} removal. Our starting set of parameter values for the present diffusion and binding model used a turnover rate of 4.0×10^{-4} ms^{-1} for the rate constant for translocation of Ca^{2+} ions from a binding site facing the cytosol to the SR lumen with simultaneous restoration of a Ca^{2+}-free pump site facing the cytosol (Scheme 1). A 50-fold increase of this turnover rate to 2.0×10^{-2} ms^{-1} caused barely noticeable changes in the time course (Fig. 6 *A*) or spatial distribution (Fig. 6 *B*) of simulated $\Delta F/F$. Thus, turnover of the pump, which follows Ca^{2+} binding to the pump and represents a relatively slow process on the time scale of a spark, has essentially no effect on the properties of the simulated sparks.

Effects of dye diffusion coefficients, kinetic constants, and concentration

In Pratusevich and Balke's (1996) model, only the diffusion of Ca^{2+} was considered, whereas the diffusion of dye (D) and Ca^{2+}-dye complex (CaD) were not considered, to sim-

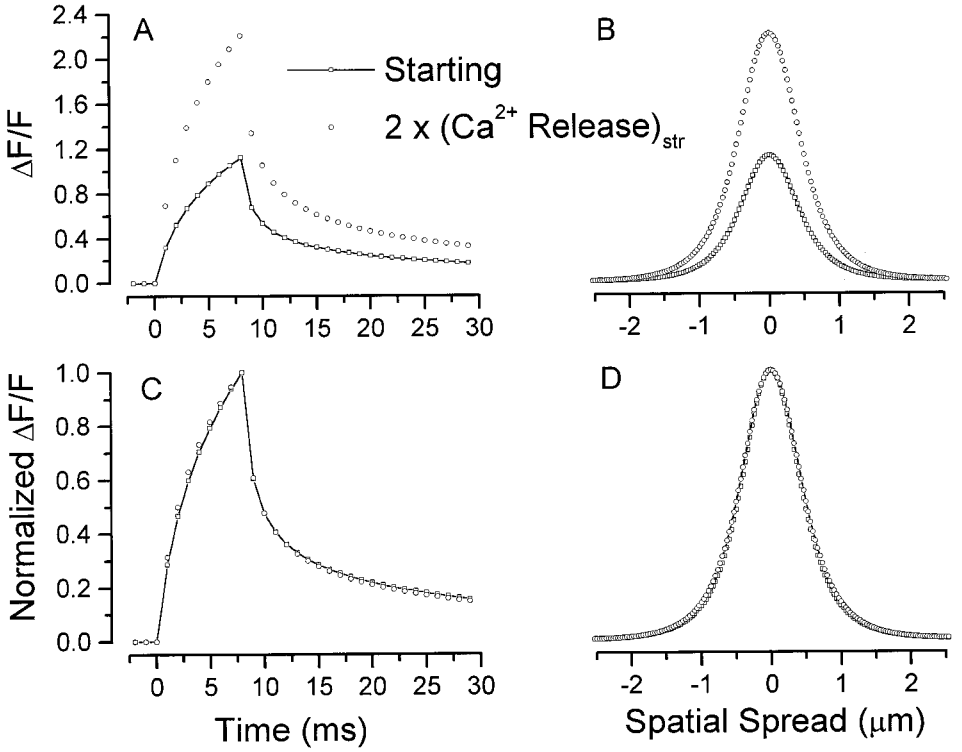

FIGURE 5 Comparisons of the results from a simulation with starting Ca^{2+} release current (□, 1.4 pA) and those from a simulation with doubled Ca^{2+} release current (○, 2.8 pA). The current duration was 8 ms in both cases. (*A*) Comparison of time courses. (*B*) Comparison of spatial spreads. (*C*) and (*D*) are (*A*) and (*B*) normalized with respect to the corresponding peak of each line.

plify the computations. To investigate the effect of diffusion of D and CaD as well as Ca^{2+} on the simulation results, we conducted a simulation with the diffusion coefficients of both D and CaD being set to zero, but with all other parameters remaining the same as those in the starting parameters. The difference between the results from the simulation with the starting parameters and those from a simulation with diffusion coefficients for D and CaD of zero

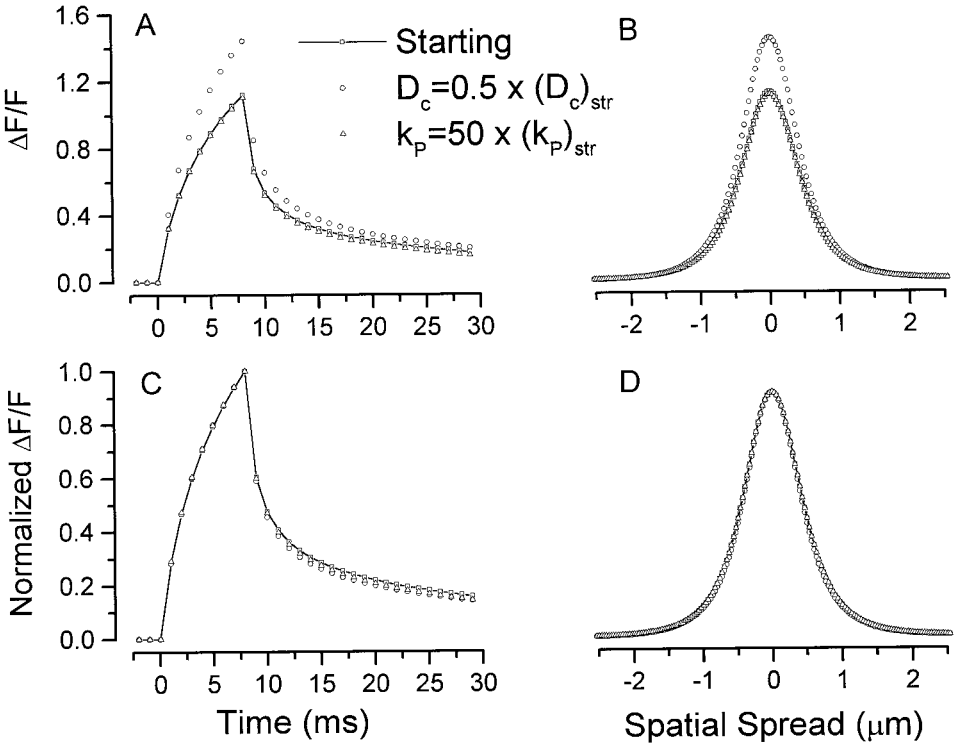

FIGURE 6 Comparisons of the results from a simulation with starting parameters (□) and those from the simulations with reduced Ca^{2+} diffusion coefficient (○, D_C was changed from 7.0×10^{-1} to 3.5×10^{-1} $\mu m^2 ms^{-1}$) and increased rate constant for translocation of Ca^{2+} ions by the SR Ca^{2+} pump (△, rate constant for translocation of Ca^{2+} was increased from 4.0×10^{-4} to 2.0×10^{-2} ms^{-1}). (*A*) Comparison of time courses. (*B*) Comparison of spatial spreads. (*C*) and (*D*) are (*A*) and (*B*) normalized with respect to the corresponding peak of each line.

were appreciable, especially on the peak amplitudes and decay time courses of the sparks, as shown in Fig. 7. Lowering the diffusion coefficients to zero greatly increased the peak of the spark (Fig. 7 *A*; compare △ to □), appreciably slowed the decay time course (Fig. 7 *C*), and slightly decreased the width of the lateral distribution of the spark (Fig. 7 *D*). It has been suggested that the diffusion coefficients of the D and CaD in myoplasm might be greater than zero but less than the theoretical value of 0.09 $\mu m^2 ms^{-1}$ used in our starting simulation (Harkins et al., 1993). Therefore, a simulation with $D_D = D_{CaD} = 0.02$ μm^2/ms, values of the diffusion coefficient of fluo-3 in myoplasm reported by Harkins et al. (1993), was also performed and is presented in Fig. 7, together with the simulations at other D_D and D_{CaD} values. The comparison in Fig. 7 clearly indicates the significant effects of the change in diffusion coefficients of D and CaD on the properties of the simulated sparks. When the values of the diffusion coefficients of D and CaD were decreased, the diffusion of CaD became slower, and the simulated spark had a higher peak and a longer FDHM but a narrower FWHM. The FDHM and FWHM of the simulated spark were thus oppositely affected by the changes in the diffusion coefficients of D and CaD.

Fluo-3 is known to bind to myoplasmic constituents in muscle fibers (Harkins et al., 1993), so it is likely that the actual concentration of dye available to bind Ca^{2+} within the fiber is higher than in the loading solution. This effect was examined in the simulations by increasing the total dye concentration two-fold compared to the starting conditions. Figure 7 shows the result of such a simulation (*inverted triangles*), the main effect being a slight reduction in the peak amplitude of the simulated spark, but with little effect on the normalized spatiotemporal properties.

Although the parameter values $D_D = D_{CaD} = 0.02$ $\mu m^2 ms^{-1}$ were selected to more closely match the expected condition within the fiber, the resulting simulation showed more deviation from the observed spark properties (Fig. 2, *C* and *D*) with regard to decay time course and spatial spread than in the starting simulation. We thus investigated whether this discrepancy might be decreased in simulations in which the rate constants for binding of Ca^{2+} to dye are made more similar to those expected in the fiber (Fig. 8). Changes in the rate constants for fluo-3 from the starting values of $k_{on,CaD} = 2.36 \times 10^{-1}$ $\mu M^{-1} ms^{-1}$ and $k_{off,CaD} = 1.75 \times 10^{-1}$ ms^{-1} (Escobar et al., 1997. $K_D = 7.4 \times 10^{-1}$ μM) were therefore also examined. The pair of different values for fluo-3 rate constants given by Harkins et al. (1993) as $k_{on,CaD} = 1.31 \times 10^{-2}$ $\mu M^{-1} ms^{-1}$ and $k_{off,CaD} = 3.35 \times 10^{-2}$ ms^{-1} ($K_D = 2.57$ μM) is examined in Fig. 8. As shown in Fig. 8 *A* (○) an 18-fold decrease in $k_{on,CaD}$ and a 5.2-fold decrease in $k_{off,CaD}$ (Harkins et al., 1993; 3.5-fold increase in K_D) greatly lowered the peak of the simulated spark. This result was partially offset by a decrease in the diffusion coefficients of D and CaD from 0.09 $\mu m^2 ms^{-1}$ to 0.02 $\mu m^2 ms^{-1}$ (△). From Fig. 8, *C* and *D*, the change in fluo-3 kinetic parameters had relatively less effect on the time course and the spatial spread though the amplitude was altered. In contrast, the change in the diffusion coefficients of D and CaD had a relatively greater effect on the time course and the spatial spread of the simulated spark (Fig. 7, *C* and *D*) than did the rate constants (Fig. 8, *C* and *D*).

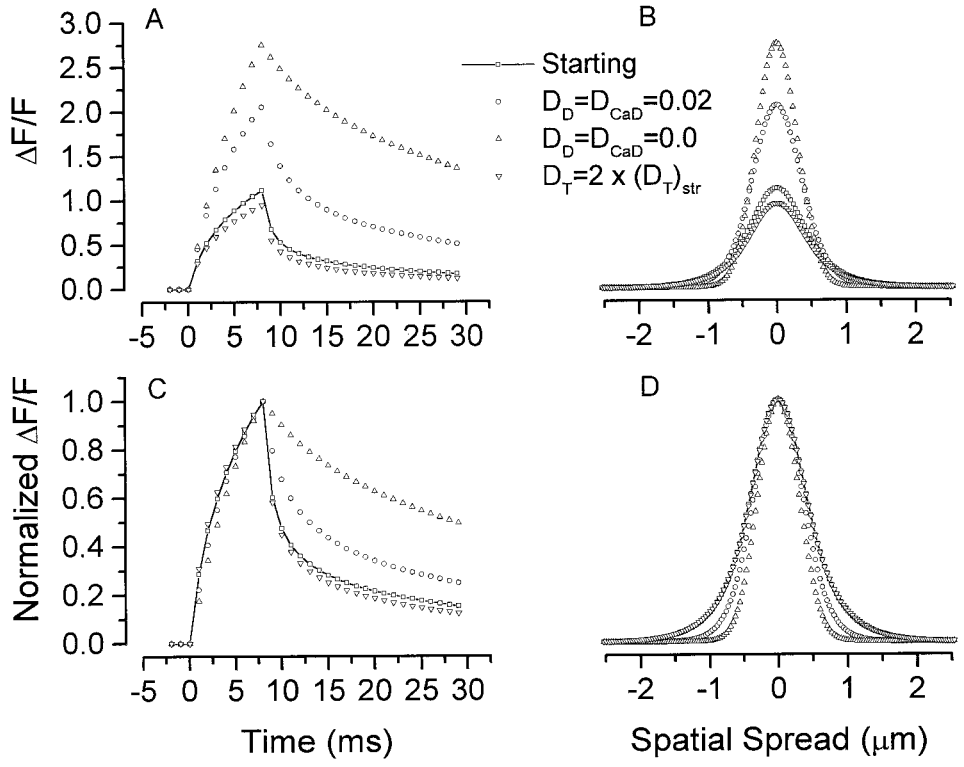

FIGURE 7 Comparisons of the results from a simulation with starting diffusion coefficients of D and CaD (□, $D_D = D_{CaD} = 9.0 \times 10^{-2}$ $\mu m^2 ms^{-1}$) and those from the simulations with smaller (○, $D_D = D_{CaD} = 2.0 \times 10^{-2}$ $\mu m^2 ms^{-1}$) or zero (△, $D_D = D_{CaD} = 0.0$) diffusion coefficients of D and CaD. ▽, simulation in which the dye concentration was increased twofold compared to the starting conditions, to 100 μM. (*A*) Comparison of time courses. (*B*) Comparison of spatial spreads. (*C*) and (*D*) are (*A*) and (*B*) normalized with respect to the corresponding peak of each line.

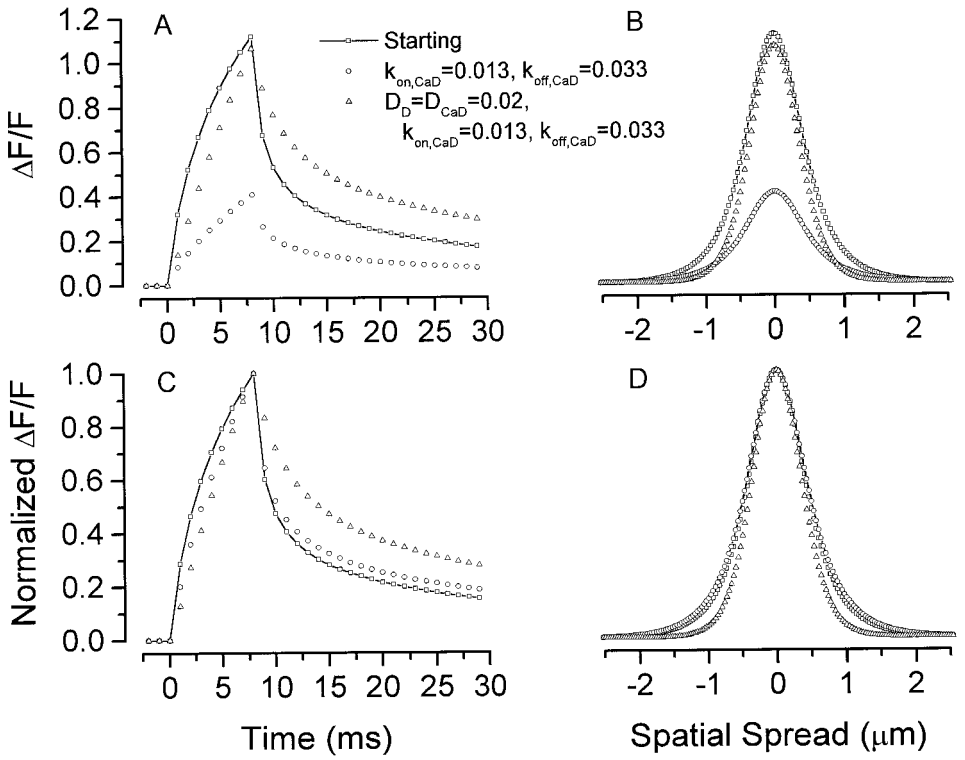

FIGURE 8 Comparison of the results under different dye kinetic properties and diffusion coefficients. □, $D_D = D_{CaD} = 9.0 \times 10^{-2}$ $\mu m^2 ms^{-1}$, $k_{on,CaD} = 2.36 \times 10^{-1}$ $\mu M^{-1} ms^{-1}$, $k_{off,CaD} = 1.75 \times 10^{-1}$ ms^{-1}. ○, $D_D = D_{CaD} = 9.0 \times 10^{-2}$ $\mu m^2 ms^{-1}$, $k_{on,CaD} = 1.3 \times 10^{-2}$ $\mu M^{-1} ms^{-1}$, $k_{off,CaD} = 3.3 \times 10^{-2}$ ms^{-1}. △, $D_D = D_{CaD} = 2.0 \times 10^{-2}$ $\mu m^2 ms^{-1}$, $k_{on,CaD} = 1.3 \times 10^{-2}$ $\mu M^{-1} ms^{-1}$, $k_{off,CaD} = 3.3 \times 10^{-2}$ ms^{-1}. (*A*) Comparison of time courses. (*B*) Comparison of spatial spreads. (*C*) and (*D*) are (*A*) and (*B*) normalized with respect to the corresponding peak of each line.

Effects of Ca^{2+} binding properties of myoplasmic sites

To investigate the effect of the Ca^{2+} binding components of the fiber on the diffusion of Ca^{2+}, a simulation with no binding sites except Ca^{2+} dye (setting $[TN]_T = [PARV]_T = [P]_T = 0.0$, $[D]_T = 50.0$ μM) was performed. Comparison of the result of this simulation (○) with that of the starting simulation (□) is given in Fig. 9. This comparison clearly demonstrates a major effect of the myoplasmic binding reactions in decreasing both the amplitude of the signals (Fig. 9, *A* and *B*) and their lateral spread (Fig. 9 *D*). The FWHM of the simulated spark without binding reactions was much larger than that of the starting spark, and very close to the mean value of the FWHM of the experimentally observed sparks (Lacampagne et al., 1996). It thus appears that one possible explanation for the lower FWHM in the starting simulation than in the experimental data could be that binding to myoplasmic sites may be less pronounced under experimental conditions than in the case of our starting parameter simulation.

Simulations were also performed to see how the spark properties are affected by the presence of the individual myoplasmic Ca^{2+} binding sites. In one such simulation, $[PARV]_T$ was set equal to zero and all other binding sites ($[TN]_T$, $[P]_T$, and $[D]_T$) were kept at the starting values. The result of this simulation is also presented in Fig. 9. As can be seen in Fig. 9, in the presence of the troponin and Ca^{2+} pump Ca^{2+}-binding sites, Ca^{2+} binding to parvalbumin had relatively little effect on either peak or FWHM. Although parvalbumin has much higher Ca^{2+} affinity ($K_D = 4.0 \times 10^{-3}$ μM) than troponin ($K_D = 1.0$ μM) or the Ca^{2+} pump, the parvalbumin sites are largely occupied by Mg^{2+} in the resting fiber, and thus make less contribution to the rapid binding of Ca^{2+}. In contrast, the removal of troponin alone or troponin together with the Ca^{2+} pump had major effects on the amplitude of the simulated sparks (Fig. 9, *A* and *B*).

In addition to the concentrations of intrinsic binding sites used in the model, the values for the rate constants of Ca^{2+} binding and unbinding to these sites also influenced the simulated sparks. In fact, a decrease in affinity of binding sites may represent a more realistic way to decrease the effects of Ca^{2+} binding sites than site elemination as in Fig. 9. The rate constants used in the starting set of parameter values correspond to literature values obtained from studies on isolated proteins (cf. Baylor et al., 1983 for tabulation). However, to reproduce the close to exponential decay of $[Ca^{2+}]$ after Ca^{2+} release in macroscopic recordings of $[Ca^{2+}]$ transients from voltage-clamped cut segments of frog skeletal muscle fibers, it was necessary to use an off-rate constant for Ca^{2+} binding to troponin C about eight-fold higher than reported for isolated proteins (Melzer et al., 1986, 1987). We thus carried out simulations in which the value of $k_{off,CaTN}$ was increased by a factor of 8 compared to the value in the starting simulation, giving an eight-fold increase in equilibrium constant for Ca^{2+}. This increase in $k_{off,CaTN}$ caused an appreciable increase in the amplitude of $\Delta F/F$ in the simulated spark (Fig. 10, *A* and *B*) reflecting the fact that a lower affinity troponin cannot compete as effectively with the dye for released Ca^{2+}. The normalized spark time course (Fig. 10 *C*) indicates that,

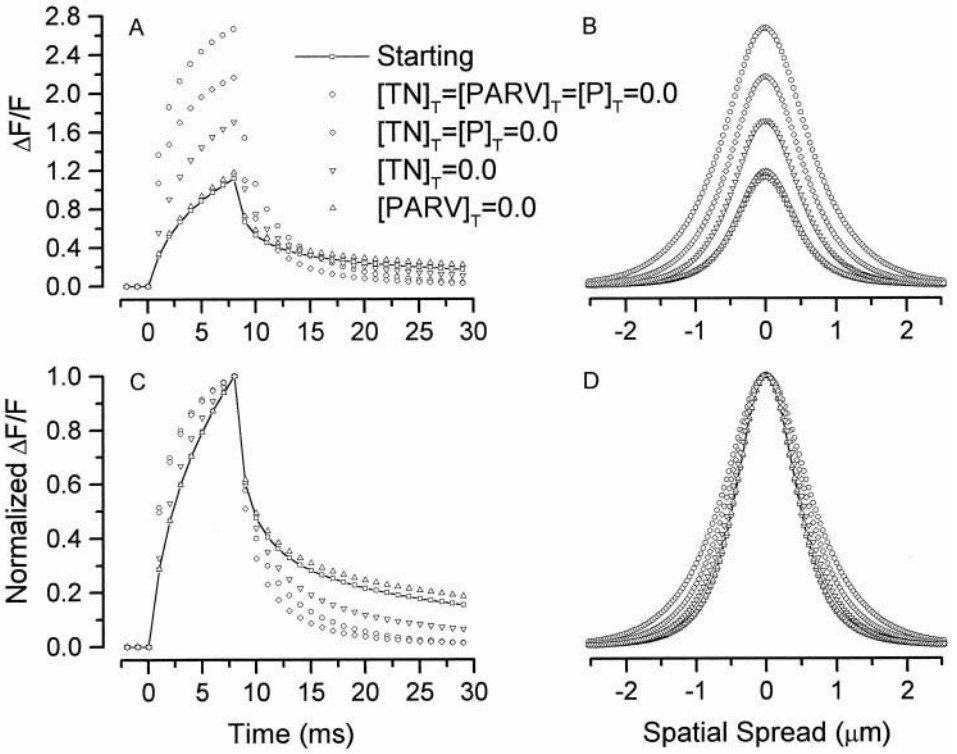

FIGURE 9 Comparisons of the results from a simulation with all starting binding sites (□, $[TN]_T$ = 240.0 μM, $[PARV]_T$ = 1000.0 μM, $[P]_T$ = 200.0 μM, $[D]_T$ = 50.0 μM) and those from simulations with the elemination of different binding sites except Ca^{2+} indicator *D* (○, $[TN]_T$ = $[PARV]_T$ = $[P]_T$ = 0.0, $[D]_T$ = 50.0 μM; ◇, $[TN]_T$ = $[P]_T$ = 0.0, $[PARV]_T$ = 1000.0 μM, $[D]_T$ = 50.0 μM; ▽, $[TN]_T$ = 0.0, $[PARV]_T$ = 1000.0 μM, $[P]_T$ = 200.0 μM, $[D]_T$ = 50.0 μM; △, $[PARV]_T$ = 0.0, $[TN]_T$ = 240.0 μM, $[P]_T$ = 200.0 μM, $[D]_T$ = 50.0 μM). (*A*) Comparison of time courses. (*B*) Comparison of spatial spreads. (*C*) and (*D*) are (*A*) and (*B*) normalized with respect to the corresponding peak of each line.

with a higher off-rate for Ca^{2+} from troponin, the decay phase of the simulated spark appears to exhibit less of the biphasic nature seen with the starting value, but instead, appears to follow more of a single exponential decay (Fig. 10 *C*). Because, in the present model, Ca^{2+} binding to the cytosol-facing sites on the SR Ca^{2+} pump exhibits very similar kinetic constants to troponin, we also decreased the off-rate constant for Ca^{2+} from the pump sites, which further accentuated the effects of changing only $k_{off,CaTN}$ (Fig. 10).

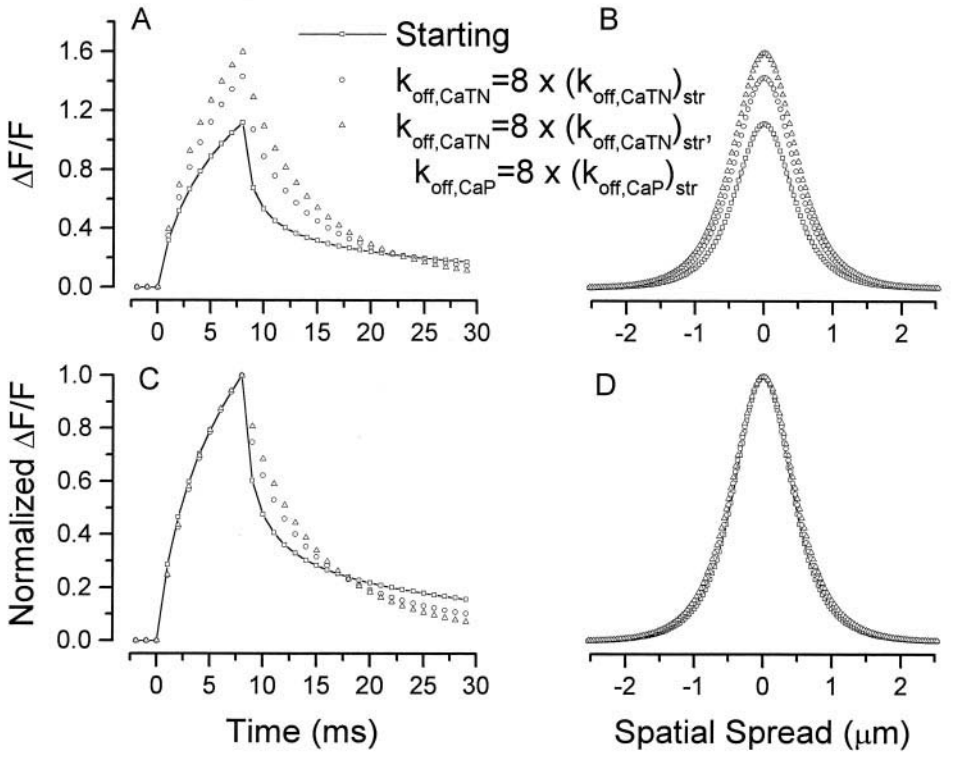

FIGURE 10 Comparisons of the results from a simulation with all starting binding properties (□) and those from simulations with increased off-rate constants for the rapidly equilibrating binding sites intrinsic to the muscle fibers (○, $k_{off,CaTN}$ was increased from 1.2×10^{-1} to 9.6×10^{-1} ms^{-1}; △, $k_{off,CaTN}$ was increased from 1.2×10^{-1} to 9.6×10^{-1} ms^{-1}, $k_{off,CaP}$ was increased from 4.0×10^{-1} to 3.2 ms^{-1}). (*A*) Comparison of time courses. (*B*) Comparison of spatial spreads. (*C*) and (*D*) are (*A*) and (*B*) normalized with respect to the corresponding peak of each line.

Effects of diffusible ATP on spark simulation

From the results presented above, it is clear that a fairly close approximation of peak, rise time, and FDHM of the experimentally observed sparks can be achieved by simulations with the current model using starting parameters. However the FWHM of simulated sparks is smaller than the mean value of the FWHM of the experimentally observed sparks (Lacampagne et al., 1996), though it is just big enough to pass the selection criterion for the experimentally recorded sparks (Klein et al., 1997).

Baylor and Hollingworth (1998) recently suggested that Ca^{2+} binding to myoplasmic ATP and diffusion of CaATP have a significant effect on intracellular Ca^{2+} movements. They reported that, in simulations of macroscopic Ca^{2+} release, the temporal half-width of simulated spatially averaged $\Delta[Ca^{2+}]$ was abnormally briefer than experimental measurements, and that the inclusion in their model of diffusible CaATP broadened the simulated temporal half-width to match the experimental results. To test if the diffusion of CaATP would tend to increase the FWHM of our simulated Ca^{2+} sparks, equations governing the binding of ATP with Ca^{2+} and the diffusion of ATP, CaATP, and MgATP were added to the equation system, Eqs. 10–25. The diffusion coefficients and binding rate constants for ATP, CaATP, and MgATP were obtained from Baylor and Hollingworth (1998). The simulation results (Fig. 11, and Table 3) show that inclusion of the diffusion components of ATP, CaATP, and MgATP in the present model had only limited effect on the FWHM.

Effect of simultaneous changes in multiple components

In the preceding figures, we have explored the effects of changes in the values of individual parameters or of 2 or 3 related parameters specifying the Ca^{2+} diffusion, Ca^{2+} binding or Ca^{2+} transport properties of various components in the model. Although most of these changes in parameter values produced relatively minor changes in the resulting simulated Ca^{2+} sparks, it is still possible that, when made together, much more major changes in the result might occur. We thus carried out a final simulation in which most of the separate changes of parameter values in the previous figures were made in the same simulation (Fig. 12; see legend for details of parameter values). This set of parameter values will be referred to as the "revised" set of model parameter values. The peak amplitude of the spark simulated with the revised set of parameter values is 35% larger than the peak for the starting parameter values (Fig. 12, *A* and *B*), but the initial rate of rise of $\Delta F/F$ is somewhat slower for the simulation with revised values (Fig. 12 *A*). The rate of decline of $\Delta F/F$ after cessation of Ca^{2+} release is slower just after the peak in the time course of the spark simulated for the revised parameters than for the starting parameters, but, by the end of the simulation period, it is decaying more rapidly (Fig. 12 *A*). Comparison of the normalized time courses shows more clearly that the rising phase of the normalized sparks is somewhat faster for the simulation using the starting parameter values than for the simulation using revised values (Fig. 12 *C*). The normalized

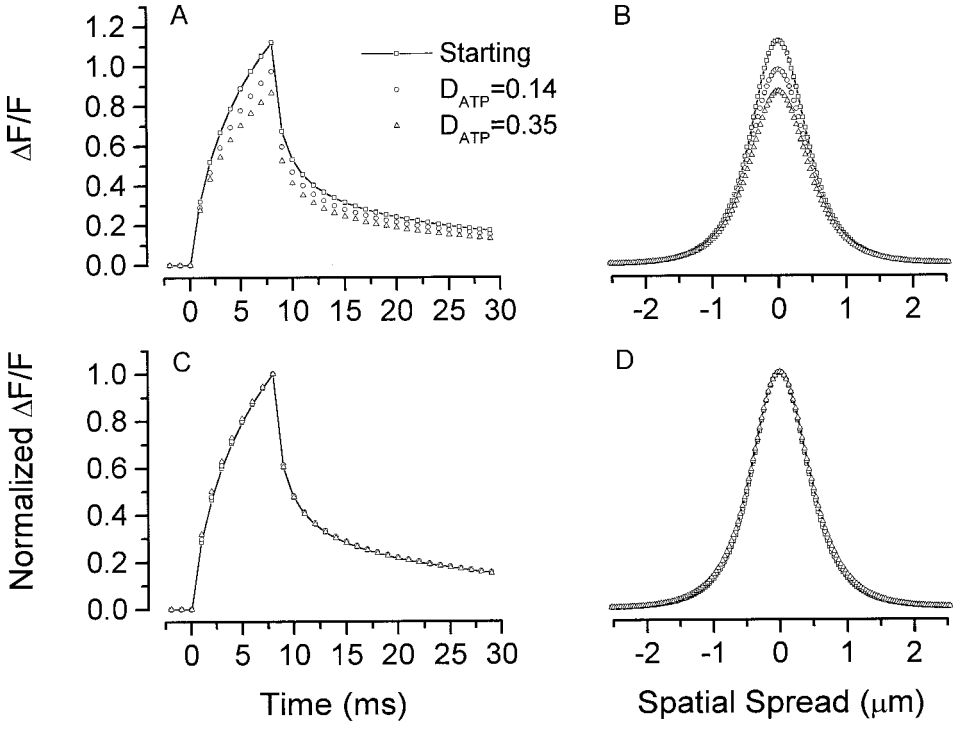

FIGURE 11 Comparisons of the results from the starting simulation, which does not include the diffusion of ATP, CaATP, and MgATP (□), and those from simulations with the diffusion of ATP, CaATP, and MgATP at two different diffusion coefficients (○, $D_{ATP} = D_{CaATP} = D_{MgATP} = 1.4 \times 10^{-1}$ $\mu m^2 ms^{-1}$; △, $D_{ATP} = D_{CaATP} = D_{MgATP} = 3.5 \times 10^{-1}$ $\mu m^2 ms^{-1}$). (*A*) Comparison of time courses. (*B*) Comparison of spatial spreads. (*C*) and (*D*) are (*A*) and (*B*) normalized with respect to the corresponding peak of each line.

TABLE 3 Spatiotemporal properties of simulated Ca^{2+} sparks

Peak*	RTime# (ms)	FDHM§ (ms)	FWHM¶ (μm)	Simulation conditions‖	Fig. no.
1.12	6.10	7.69	1.00	Starting values	2
2.21	5.88	7.81	1.01	$I = 2 \times I_{str}$	5
1.44	6.03	7.48	0.96	$D_C = 0.5 \times (D_C)_{str}$	6
1.10	6.01	7.67	1.00	$k_P = 50 \times (k_P)_{str}$	6
1.47	6.03	8.80	1.03	$k_{off,CaTN} = 10 \times (k_{off,CaTN})_{str}$	–
2.75	6.24	25.70	0.72	$D_{CaD} = D_D = 0.0$	7
2.06	6.10	10.39	0.89	$D_{CaD} = D_D = 0.02\ \mu m^2 ms^{-1}$	7
0.95	5.83	7.58	0.97	$[D]_T = 2 \times ([D]_T)_{str}$	7
0.41	6.36	7.27	1.03	$k_{on,CaD} = 0.0131\ \mu M^{-1} ms^{-1}$ $k_{off,CaD} = 0.0335\ ms^{-1}$	8
1.06	6.24	10.39	0.85	$D_{CaD} = D_D = 0.02\ \mu m^2 ms^{-1}$ $k_{on,CaD} = 0.0131\ \mu M^{-1} ms^{-1}$ $k_{off,CaD} = 0.0335\ ms^{-1}$	8
1.47	6.03	12.96	0.91	$D_{CaD} = D_D = 0.02\ \mu m^2 ms^{-1}$ $k_{on,CaD} = 0.0131\ \mu M^{-1} ms^{-1}$ $k_{off,CaD} = 0.0335\ ms^{-1}$ $k_{off,CaTN} = 10 \times (k_{off,CaTN})_{str}$	–
2.67	4.64	8.60	1.40	$[TN]_T = [PARV]_T = [P]_T = 0.0$	9
1.36	5.96	7.90	1.04	$[PARV]_T = [P]_T = 0.0$	–
1.18	6.08	7.81	0.98	$[PARV]_T = 0.0$	9
1.70	5.61	7.83	1.09	$[TN]_T = 0.0$	9
1.12	6.14	7.58	0.97	$[Mg^+]_0 = 650.0\ \mu M$	–
1.43	5.94	8.99	1.01	$k_{off,CaTN} = 8 \times (k_{off,CaTN})_{str}$	10
1.60	6.01	9.75	1.09	$k_{off,CaTN} = 8 \times (k_{off,CaTN})_{str}$ $k_{off,CaP} = 8 \times (k_{off,CaP})_{str}$	10
0.97	6.03	7.83	1.02	$D_{ATP} = 0.14\ \mu m^2 ms^{-1}$ $D_{CaATP} = D_{MgATP} = D_{ATP}$	11
0.87	5.89	7.9	1.03	$D_{ATP} = 0.35\ \mu m^2 ms^{-1}$ $D_{CaATP} = D_{MgATP} = D_{ATP}$	11
1.51	6.15	13.34	0.87	$D_C = 0.5 \times (D_C)_{str}$ $D_{CaD} = D_D = 0.02\ \mu m^2 ms^{-1}$ $k_{on,CaD} = 0.0131\ \mu M^{-1} ms^{-1}$ $k_{off,CaD} = 0.0335\ ms^{-1}$ $k_{off,CaTN} = 8 \times (k_{off,CaTN})_{str}$ $D_{ATP} = 0.14\ \mu m^2 ms^{-1}$ $D_{CaATP} = D_{MgATP} = D_{ATP}$	12

*Peak, the difference between the maximum and resting ratio values.
#RTime, rise time, time to go from 10 to 90% of peak value.
§FDHM, full duration at half maximum.
¶FWHM, full width at half maximum.
‖Only values changed from starting conditions are listed.

time courses also show that the simulation with the starting values exhibits a biphasic time course of decay, whereas the simulation with revised values is closer to a single exponential time course (Fig. 12 *C*). The temporal duration for the simulation with the revised parameters (FDHM = 13.3 ms) is closer to the experimental mean value of 11 ms (Klein et al., 1997) than the 7.7 ms obtained with the starting parameter values. However, the relative spatial spread of fluorescence is slightly less wide for the revised parameters (FWHM = 0.87) than for the starting parameters (FWHM = 1.00, Fig. 12 *D*).

Tabulation of results of various simulations

Table 3 presents a collection of the peak, rise time, FDHM, and FWHM from simulated sparks using a range of parameter values. Figure numbers for simulations presented graphically are indicated in the table. From the data in this table it is evident that changing parameters for the simulation had a much bigger effect on the peak of the spark than on the rise time, FDHM, or FWHM. Changes of most parameters have little influence on the rise time of the calculated Ca^{2+} sparks. The diffusion coefficients of D and CaD have significant effects on the FDHM and the FWHM of the calculated Ca^{2+} sparks.

DISCUSSION AND CONCLUSION

Specification of the model

To better interpret the formation and underlying mechanism of experimentally observed Ca^{2+} sparks, a 3D theoretical model was built to simulate numerically the Ca^{2+} sparks in skeletal muscle using a finite difference method. The model

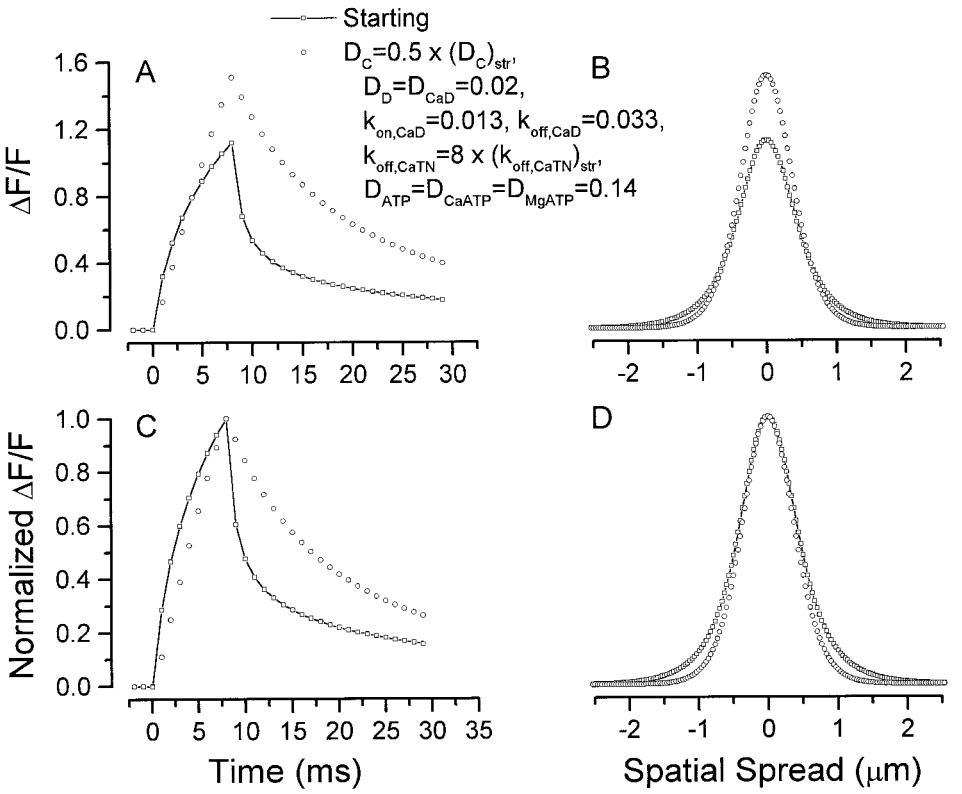

FIGURE 12 Comparisons of the results from a simulation with the starting parameters (□) and those from a simulation with several simultaneous parameter changes made separately in the previous comparisons, and including the diffusion of ATP, CaATP, and MgATP (○, D_C was changed from 7.0×10^{-1} to 3.5×10^{-1} $\mu m^2 ms^{-1}$, D_D and D_{CaD} from 9.0×10^{-2} to 2.0×10^{-2} $\mu m^2 ms^{-1}$, $k_{on,CaD}$ from 2.36×10^{-1} to 1.3×10^{-2} $\mu M^{-1} ms^{-1}$, and $k_{off,CaD}$ from 1.75×10^{-1} to 3.3×10^{-2} ms^{-1}, $k_{off,CaTN}$ from 1.2×10^{-1} to 9.6×10^{-1} ms^{-1}, and $D_{ATP} = D_{CaATP} = D_{MgATP} = 1.4 \times 10^{-1}$ $\mu m^2 ms^{-1}$). (*A*) Comparison of time courses. (*B*) Comparison of spatial spreads. (*C*) and (*D*) are (*A*) and (*B*) normalized with respect to the corresponding peak of each line.

was based on the sarcomere structure and the well characterized Ca^{2+} binding properties of the sarcomere in skeletal muscle. Many initial ideas in building the present model were drawn from the models of Cannell and Allen (1984) and of Pratusevich and Balke (1996). In developing the current simulation model, enhancements were made in the 3D physical configuration of the distribution of specific binding components, use of a graded network and parallel processing for faster solution of the equation system. The main differences of the present model from that of Cannell and Allen's (1984) model are the Ca^{2+} releasing source and the specification of the simulation space. Cannell and Allen (1984) intended to simulate activation of large numbers of release sites in a skeletal muscle fiber and thus assumed uniform Ca^{2+} flux along the entire junctional SR. In contrast, to generate an isolated [Ca^{2+}] elevation, or Ca^{2+} spark, a point source was used by Pratusevich and Balke (1996). The simulation space was extended in the present article from a single sarcomere and 2D setup, which was appropriate to Cannell and Allen's simulated uniform activation, to a 12-sarcomere 3D setup to accommodate the spatial spread of the spark and the asymmetrical distribution of binding sites around the point source. However, this extended simulation space was restricted to a much smaller one than that used by Pratusevich and Balke (1996) so that small, slow changes in Ca^{2+} far from the release site were not considered; this configuration permitted a much finer grid network to be used in the solution of the differential equation system with improved computational accuracy. A graded grid network and parallel computation were used to handle effectively the increased computational load due to the large number of grid points discretized in the computational space. Consideration of the diffusion of D and CaD in the current model was an important development compared to Pratusevich and Balke's approach.

Comparison of properties of simulated and experimentally observed sparks

An ultimate goal in simulating Ca^{2+} sparks is to reproduce closely the characteristics of experimentally recorded sparks in an effort to deduce the properties of the Ca^{2+} release source underlying each spark, as well as to characterize the myoplasmic Ca^{2+} binding and diffusion properties of the muscle fiber. A detailed comparison of individual experimental and simulated sparks, including adjustment of model parameter values to most closely reproduce an individual experimentally recorded spark, is beyond the scope of the present paper. However, we can compare the characteristics of the sparks simulated here with the average values of properties of experimentally recorded Ca^{2+} sparks. Table 4 presents average values of spark properties for use in such comparisons. The values in Table 4 were obtained from analysis of relatively large numbers of sparks recorded using the same confocal system in our laboratory under several experimental conditions.

The amplitude of a spark is of central interest for addressing the question of the number of channels that may be active in generating the spark. Except for the series of

TABLE 4 Mean values of spatiotemporal properties of experimentally recorded Ca^{2+} sparks

Peak*	RTime[#] (ms)	FDHM[§] (ms)	FWHM[¶] (μm)	n[‖]	N**	Act.[##]	References and figure no.
0.89 ± 0.03		14.8 ± 0.3	1.51 ± 0.10	1168	4	V	Lacampagne et al., 1996 (Fig. 4)
0.85 ± 0.01	5.9 ± 0.2			722	1	V	Klein et al., 1997 (Fig. 5)
0.83 ± 0.02[§§]	5.0 ± 0.1[§§]			195	11	V	Klein et al., 1999 (Fig. 12)
0.81 ± 0.05[¶¶]	5.3 ± 0.1[¶¶]	9.5 ± 0.3[¶¶]	1.73 ± 0.13[¶¶]	1396	10	L	Lacampagne et al., 1998 (Fig. 7)
0.75 ± 0.02[§§]	5.1 ± 0.1[§§]			122	6	L	Klein et al., 1999 (Fig. 12)

*Peak, the difference between the maximum and resting ratio values.
[#]RTime, rise time, time to go from 10 to 90% of peak value.
[§]FDHM, full duration at half maximum.
[¶]FWHM, full width at half maximum.
[‖]n, total number of sparks analyzed.
**N, number of fibers from which analyzed sparks were recorded.
[##]Act, mechanisms of spark activation: V, voltage activated; L, spontaneous sparks, presumably ligand activated.
[§§]Values from sparks in repetitive mode trains.
[¶¶]All [Mg^{2+}] included.

simulations examining the effect of current magnitude on the properties of the simulated spark, all other simulations presented here use a 1.4 pA point source of current, with the current duration being 8 ms in all simulations. The 1.4-pA current was previously selected to approximate the current through a single SR Ca^{2+} release channel (Pratusevich and Balke, 1996). Thus, the extent to which the amplitudes of the sparks simulated here agree with the experimentally observed spark amplitudes provides potential information regarding the likelihood that current through a single SR Ca^{2+} channel could generate a spark.

The spark simulated with the starting parameter values and a current of 1.4 pA has a slightly larger amplitude than the range of mean values of experimentally observed spark amplitudes (Table 4). However, the average experimental values underestimate the average value of sparks arising on the scan line because the average experimental values include sparks, which are underestimated in amplitude due to their origination at a point removed from the scan line location (Fig. 4). Thus, it may be more appropriate to consider the largest experimentally observed sparks, which must both originate close to the scan line and correspond to the largest actual Ca^{2+} releases. Since individual Ca^{2+} sparks having amplitudes several times the average values in Table 4 have been observed and because the amplitude of a simulated spark varies almost directly with the current magnitude (Fig. 5), it is possible that the Ca^{2+} current underlying the largest experimentally observed sparks could be several-fold larger than the 1.4 pA used in the present simulations. Furthermore, if the release duration were shorter than the 8 ms used here (Lacampagne et al., 1999), the current magnitude would have to be even further increased. Finally, the current through a single SR Ca^{2+} release channel could be lower than 1.4 pA (Mejía-Alvarez et al., 1999). Thus, the release current required to simulate large sparks could conceivably exceed the maximum current that could reasonably be expected through a single SR Ca^{2+} release channel. This would indicate that more than one channel may be involved in generating a spark. In contrast, it is important to note that the value of $\Delta F/F$ in a spark depends on both the increase of fluorescence (ΔF) during the spark and on the resting fluorescence (F) in the fiber. Thus, if F were decreased due to decreased resting myoplasmic [Ca^{2+}] at constant fluo-3 concentration, a given Ca^{2+} release would produce approximately the same ΔF, but a larger value of peak $\Delta F/F$. Some of the largest values of peak $\Delta F/F$ in experimentally observed sparks might thus corresponded to situations of decreased F. Furthermore, if the myoplasmic Ca^{2+} binding sites are less effective than specified by the starting parameter values (cf., Figs. 9 and 10), the amplitude of the simulated spark could also be larger for the same release current. Given these various possible opposing influences on spark amplitudes, the present simulations cannot be considered to be obviously inconsistent with the possibility that current through a single SR Ca^{2+} release channel could underlie an experimentally observed Ca^{2+} spark.

The duration of the rising phase of a simulated spark depends on the duration of the Ca^{2+} release current assumed to underlie the spark (Fig. 2 *A*). Using the present starting parameter values, an 8-ms duration was selected for the Ca^{2+} release current to produce a simulated spark having a rise time (6.1 ms) close to the range of values of average experimentally observed rise time (5.0–5.9 ms, Table 4; note that rise time is defined as the time to go from 10 to 90% of peak spark amplitude for both the present simulations and for the experimental values in Table 4). All subsequent simulations were carried out using the same 8-ms duration Ca^{2+} release current, and the simulated rise times (Table 3) were always close to the experimental range. Thus, appropriate selection of the release current duration can provide simulations with rise times close to those observed experimentally.

The temporal and spatial extent of a spark, specified as the FDHM and the FWHM, respectively, are the two remaining spark properties to be examined. For the spark simulated with the starting set of parameter values, the FDHM was 7.7 ms, which is somewhat lower than the two

average values (9.5 and 14.8 ms) from experimental sparks presented in Table 4. Decreasing the diffusion constant for fluo-3 from 0.09 to 0.02 $\mu m^2 ms^{-1}$, a value that is more likely to apply to the myoplasmic environment (Harkins et al., 1993), gives a simulated spark with FDHM within the experimental range of average values. The spatial FWHM of the starting simulation (1.00 μm) is well below the two experimental average values (1.51 and 1.73 μm) in Table 4. Decreasing the fluo-3 diffusion constant gives simulated sparks with even lower values of FWHM. The present simulations systematically give lower values of spatial half width than the experimental average values, which is one of the major inconsistencies between the present simulations and the experimentally observed sparks.

The limitations of the present model that give rise to the discrepancy between simulated and experimentally observed values for FWHM remain to be established. One possibility might be that the simulated light collection properties of the confocal system, which already provide a significant distortion of the actual spatial distribution of fluorescence (Fig. 2), do not correspond with the experimental situation. The optical distortion under experimental conditions might have been even larger than simulated here. Alternatively, if multiple channels are involved in the Ca^{2+} release underlying a spark, it might be possible that the actual spatial extent of the current source generating a spark might have to be larger than the single voxel assumed in the present simulations.

Spark amplitude increases in direct proportion to the magnitude of the underlying Ca^{2+} release current

The magnitude of the current source assumed to be generating a Ca^{2+} spark will obviously be a crucial factor in determining the amplitude of the simulated spark. We have found that, if the magnitude of an assumed 8-ms duration source current is doubled from 1.4 to 2.8 pA, the peak amplitude of the resulting simulated Ca^{2+} spark is also doubled (Fig. 5, *A* and *B*) when using the starting set of values for the diffusion and binding properties in the model. Furthermore, the amplitude of the simulated $\Delta F/F$ was also doubled at all times and at all spatial locations (Fig. 5, *C* and *D*). This proportionality between the source current and the resulting change in fluorescence is as expected for a system in which the dissipation of Ca^{2+} ions from the release source is primarily determined by diffusion, which is a linear process. Furthermore, for relatively brief elevations of myoplasmic [Ca^{2+}], as occur during a Ca^{2+} spark, the various Ca^{2+} binding sites may also not change significantly in Ca^{2+} occupancy, in which case, Ca^{2+} binding would also be roughly proportional to the release magnitude. Thus, the observed doubling of spark amplitude with source current magnitude would be consistent with diffusion and binding being effectively linear processes during a Ca^{2+} spark. However, even though doubling the magnitude of the release current doubles the signal at all locations and times, it should be noted that such doubling of absolute amplitudes does not alter the values of the parameters FDHM and FWHM, which depend on relative rather than absolute amplitudes. Thus, simply altering the release current magnitude cannot correct any discrepancy between simulated and observed FDHM and FWHM.

The total amount of Ca^{2+} released in a spark is given by the integral of the concentrations of free and bound Ca^{2+} over the entire volume occupied by the spark (Sun et al., 1998) providing that Ca^{2+} transport is negligible. Based on this volume integral concept, it might at first appear that spark amplitude should only increase in proportion to the cube root of the release current magnitude (Sun et al., 1998). However, considering the simplest case of a linear system, it is clear that the amplitude of a spark should be directly proportional to the magnitude of the release current that generates the spark. In such a linear system, if the magnitude of the release current were to increase from i to $K \times i$, where K is a constant, then free and bound Ca^{2+} will also increase at each location and at each time by the factor K. The volume integral of free and bound Ca^{2+}, which corresponds to the amount of Ca^{2+} released for the release current magnitude $K \times i$, would then simply be K times the volume integral for the release current i. Following this reasoning, and the results of our simulations, the relative magnitude of the release current underlying a spark should be approximately proportional to the relative amplitudes of the resulting sparks if the release current durations are the same. Thus, the amplitude of a spark and the integral of free and bound Ca^{2+} over the spark volume will both be proportional to release current magnitude for a constant duration current. These considerations are obviously of central importance when using relative changes in observed spark amplitudes to deduce information concerning the relative magnitudes of the underlying currents that generated the observed sparks.

Effects of altering various model parameter values

Numerous simulations with different variations from the starting parameter values were performed to investigate the effects of the changes of those parameters on the properties of simulated sparks. In agreement with other investigators (Pratusevich and Balke, 1996; Ríos et al., 1998) the FWHM of our starting spark was narrower than the mean FWHM of experimentally observed sparks. Therefore, the changes of parameters that could result in the FWHM of the simulated spark becoming wider was a significant factor in evaluating the results of many of our simulations with variations of parameters.

From Figs. 7 and 9, it is clear that the two main factors affecting the spatial spread of Ca^{2+} are the diffusion coefficients of D and CaD and the binding reactions of Ca^{2+} with binding sites. As can be seen from Fig. 7, *C* and *D*, the

smaller the diffusion coefficients of D and CaD, the narrower the spatial spread, and the slower the decay of [CaD] became. Thus, changes in these diffusion coefficients have opposite effects on the spatial spread and the temporal decay of Ca^{2+} sparks. When the diffusion coefficients of D and CaD were set to zero, the spatial spread of the spark was significantly limited and its decay time course was much slower. This result clearly indicated that the inclusion of the diffusion terms of D and CaD in the simulation of Ca^{2+} spark is not only more intuitively reasonable, but also produces the simulated sparks that more closely resemble experimentally recorded sparks.

The comparison presented in Fig. 9 quantitatively shows the very significant amount of Ca^{2+} binding to the binding sites and the significant effect of the binding reactions on the diffusion of Ca^{2+}. The difference between the starting peak and the peak without any binding sites is more than 100% of the peak of the starting spark (Fig. 9, *A* and *B*). In the absence of Ca^{2+} binding to troponin, parvalbumin, and the SR Ca^{2+} pump, the fluorescence level at the end of the simulation was also lower than that with binding (Fig. 9 *C*). The spatial spread was obviously wider without binding than with binding (Fig. 9 *D*). The FWHM of the simulated spark with no binding to troponin, parvalbumin, or pump was 1.4 μm (Fig. 9 *B* and Table 3), which is close to the mean FWHM of the experimentally recorded sparks (Table 4). However, the total absence of binding sites is an unreasonable assumption.

It has recently been suggested that the diffusion of CaATP may have a significant effect on Ca^{2+} spread during macroscopic activation of Ca^{2+} release in muscle (Baylor and Hollingworth, 1998). However, we did not observe any significant broadening of FWHM by adding the diffusion terms of ATP, CaATP, and MgATP to our present model (Fig. 11). A possible explanation of why the diffusion of CaATP, MgATP, and ATP had very limited effects on the FWHM of the microscopic release events in our simulation may be that the current model included all major diffusion and binding components that are the actual major factors affecting FWHM. As we have shown in Figs. 7 and 9, when the diffusion of D and CaD was absent or the binding components were present in the simulation, the FWHM was significantly reduced. This may indirectly indicate that any model with fewer diffusible components or more binding components may produce a wider FWHM when the diffusion of CaATP is considered.

Effects of confocal line locations

Our results confirm the conclusion of Pratusevich and Balke (1996) that both defocus and lateral displacement of the scan line have significant influence on the amplitude (peak) of the sparks but not on the rise time. Figure 4 *A* shows that the rise times of the time courses at all six scan-line locations are essentially the same, about 80% (6 ms) of the Ca^{2+} release duration (8 ms), and thus independent of their amplitudes. In other words, the rise time of a spark is hardly affected by the positions of the scan lines. The rise times are also essentially the same for most of the simulations with different simulation parameters (Table 3). Our simulations indicated that the rise time is mainly determined by the duration of the Ca^{2+} release underlying the Ca^{2+} spark. We used an efflux duration of 8 ms to make the rise time of simulated sparks similar to the average rise time (equal to 10–90% of peak) of experimentally measured sparks (Klein et al., 1997). From Figs. 4, *C* and *D*, it is obvious that the shapes of the spatial spreads from the sparks scanned at these six positions are very similar, and the shapes of the times courses for these positions are also quite similar but with a tendency to become slower in the decay phase, when the scan line is moved farther away from the Ca^{2+} releasing source.

In experimentally recorded images of sparks, there are smaller Ca^{2+} elevation events in addition to identified sparks. Some of these smaller events may correspond to Ca^{2+} sparks recorded at the scan line positions representing a displacement >0.5 μm or a defocus >1.0 μm, i.e., those scanned at lines 3, 4, 5, and 6 in Fig. 4. However, it is possible that not all of these smaller events are large sparks viewed at a displacement or defocus. It has been suggested that such smaller events may be due to release not constituted by sparks (Shirokova and Ríos, 1997). Alternatively, small events could arise from briefer open duration than simulated here, with the release source located on the scan line.

Future directions

Possibilities for further investigation of Ca^{2+} sparks using the current model exist in several aspects. With appropriate modification and enhancement, the current model could be used in the investigation of alternative possible spatial and temporal calcium-releasing patterns underlying the Ca^{2+} spark. The releasing pattern may be an important factor affecting the spatial spread of the Ca^{2+} spark. It has been suggested by Ríos et al. (1998) that the narrower FWHM of the computed spark might indicate that the real Ca^{2+} release source might have nonnegligible dimensions. A direct measurement of the PSF of the confocal microscope combined for the position of the muscle fiber in our chamber with a detailed error analysis of the confocal measuring system may provide more accurate information for the simulation than obtained with the Gaussian kernel used as our approximation to the microscope PSF as used in the present simulation. The accuracy of the rate constants for the Ca^{2+} binding sites seems to be another very important area for future investigation because different values of rate constants have been used in different modeling studies. In addition to two pairs of values used in current simulation, the rate constants for the reaction of Ca^{2+} and fluo-3 have also been assumed as $k_{on,CaD} = 1 \times 10^{-1}$ $\mu M^{-1} ms^{-1}$ and $k_{off,CaD} = 1 \times 10^{-1}$ ms^{-1} (Ríos et al., 1998). Any new

experimental evidence about the kinetic rate constants of the binding components in the model can serve as the new input for future simulations. Additional Ca^{2+} binding components, such as EGTA, might also be considered in the future.

In conclusion, a close simulation of the Ca^{2+} sparks experimentally observed in skeletal muscle can be achieved by the present numerical simulation model. The simulations by this model clearly showed the effects of changes of many parameters, such as the diffusion coefficients of the D and CaD, the kinetic rate constants of fluo-3, and the positions of the scan line, on the properties of the Ca^{2+} spark. The present model provides possibilities for further investigation of parameters, which are significant to the investigation of Ca^{2+} movements underlying Ca^{2+} sparks in skeletal muscle.

APPENDIX A: FINITE DIFFERENCE EQUATIONS

The time derivative and spatial derivatives in Eqs. 10–19 are approximated by forward and central finite divided differences, respectively (Chapra and Canale, 1988). The accuracy of these approximations is first-order in time and second-order in space (Pozrikidis, 1997). Because even-sided cubes were used as the grid elements in the computational domain the accuracies of the spatial approximation in three coordinate directions were the same.

Using subscripts m, i, j, k to represent the temporal (m) and spatial indexes (i, j, k) of a variable at time m and grid point i, j, k, Δt to represent the time increment and Δx, Δy, and Δz to represent the spatial steps, respectively, the difference equations for Eqs. 10–19 are:

General equation

$$[Ca^{2+}]_{m+1,i,j,k} = [Ca^{2+}]_{m,i,j,k} + \Delta t\left(\frac{\partial[Ca^{2+}]}{\partial t}\right)_{m,i,j,k} \tag{43}$$

$$F_{m,i,j,k} = \left(\frac{d[CaTN]}{dt}\right)_{m,i,j,k} + \left(\frac{d[CaPARV]}{dt}\right)_{m,i,j,k} + \left(\frac{d[CaP]}{dt}\right)_{m,i,j,k} + \left[\left(\frac{d[CaD]}{dt}\right)_F\right]_{m,i,j,k} + V_{m,i,j,k} - L_{m,i,j,k} \tag{44}$$

Binding equations

$$[CaTN]_{m+1,i,j,k} = [CaTN]_{m,i,j,k} + \Delta t\left(\frac{d[CaTN]}{dt}\right)_{m,i,j,k} \tag{45}$$

$$[CaPARV]_{m+1,i,j,k} = [CaPARV]_{m,i,j,k} + \Delta t\left(\frac{d[CaPARV]}{dt}\right)_{m,i,j,k} \tag{46}$$

$$[CaP]_{m+1,i,j,k} = [CaP]_{m,i,j,k} + \Delta t\left(\frac{d[CaP]}{dt}\right)_{m,i,j,k} \tag{47}$$

$$[D]_{m+1,i,j,k} = [D]_{m,i,j,k} + \Delta t\left(\frac{\partial[D]}{\partial t}\right)_{m,i,j,k} \tag{48}$$

$$[CaD]_{m+1,i,j,k} = [CaD]_{m,i,j,k} + \Delta t\left(\frac{\partial[CaD]}{\partial t}\right)_{m,i,j,k} \tag{49}$$

$$([CaD]_F)_{m+1,i,j,k} = ([CaD]_F)_{m,i,j,k} + \Delta t\left(\frac{d[CaD]_F}{dt}\right)_{m,i,j,k} \tag{50}$$

Pump transport and leak

$$V_{m,i,j,k} = k_P[CaP]_{m,i,j,k} \tag{51}$$

$$L_{m,i,j,k} = k_P[CaP]_{0,i,j,k} \tag{52}$$

where

$$\left(\frac{\partial[Ca^{2+}]}{\partial t}\right)_{m,i,j,k} = D_C\left[\frac{[Ca^{2+}]_{m,i+1,j,k} - 2[Ca^{2+}]_{m,i,j,k} + [Ca^{2+}]_{m,i-1,j,k}}{(\Delta x)^2} + \frac{[Ca^{2+}]_{m,i,j+1,k} - 2[Ca^{2+}]_{m,i,j,k} + [Ca^{2+}]_{m,i,j-1,k}}{(\Delta y)^2} + \frac{[Ca^{2+}]_{m,i,j,k+1} - 2[Ca^{2+}]_{m,i,j,k} + [Ca^{2+}]_{m,i,j,k-1}}{(\Delta z)^2}\right] - F_{m,i,j,k} \tag{53}$$

$$\left(\frac{d[CaTN]}{dt}\right)_{m,i,j,k} = k_{on,CaTN}[Ca^{2+}]_{m,i,j,k}\{[TN]_T - [CaTN]_{m,i,j,k}\} - k_{off,CaTN}[CaTN]_{m,i,j,k} \tag{54}$$

$$\left(\frac{d[CaPARV]}{dt}\right)_{m,i,j,k} = k_{on,CaPARV}[Ca^{2+}]_{m,i,j,k}\{[PARV]'_T - [CaPARV]_{m,i,j,k}\} - k_{off,CaPARV}[CaPARV]_{m,i,j,k} \tag{55}$$

$$\left(\frac{d[CaP]}{dt}\right)_{m,i,j,k} = k_{on,CaP}[Ca^{2+}]_{m,i,j,k}\{[P]_T - [CaP]_{m,i,j,k}\} - (k_{off,CaP} + k_P)[CaP]_{m,i,j,k} \tag{56}$$

$$\left(\frac{\partial[D]}{\partial t}\right)_{m,i,j,k} = D_D\left[\frac{[D]_{m,i+1,j,k} - 2[D]_{m,i,j,k} + [D]_{m,i-1,j,k}}{(\Delta x)^2} + \frac{[D]_{m,i,j+1,k} - 2[D]_{m,i,j,k} + [D]_{m,i,j-1,k}}{(\Delta y)^2} + \frac{[D]_{m,i,j,k+1} - 2[D]_{m,i,j,k} + [D]_{m,i,j,k-1}}{(\Delta z)^2}\right] + k_{off,CaD}[CaD]_{m,i,j,k} - k_{on,CaD}[Ca^{2+}]_{m,i,j,k}[D]_{m,i,j,k} \tag{57}$$

$$\left(\frac{\partial[\mathrm{CaD}]}{\partial t}\right)_{\mathrm{m,i,j,k}} = D_{\mathrm{CaD}}\left[\frac{[\mathrm{CaD}]_{\mathrm{m,i+1,j,k}} - 2[\mathrm{CaD}]_{\mathrm{m,i,j,k}} + [\mathrm{CaD}]_{\mathrm{m,i-1,j,k}}}{(\Delta x)^2} + \frac{[\mathrm{CaD}]_{\mathrm{m,i,j+1,k}} - 2[\mathrm{CaD}]_{\mathrm{m,i,j,k}} + [\mathrm{CaD}]_{\mathrm{m,i,j-1,k}}}{(\Delta y)^2} + \frac{[\mathrm{CaD}]_{\mathrm{m,i,j,k+1}} - 2[\mathrm{CaD}]_{\mathrm{m,i,j,k}} + [\mathrm{CaD}]_{\mathrm{m,i,j,k-1}}}{(\Delta z)^2}\right] + k_{\mathrm{on,CaD}}[\mathrm{Ca}^{2+}]_{\mathrm{m,i,j,k}}[\mathrm{D}]_{\mathrm{m,i,j,k}} - k_{\mathrm{off,CaD}}[\mathrm{CaD}]_{\mathrm{m,i,j,k}} \quad (58)$$

$$\left[\left(\frac{\mathrm{d}[\mathrm{CaD}]}{\mathrm{d}t}\right)_{\mathrm{F}}\right]_{\mathrm{m,i,j,k}} = k_{\mathrm{on,CaD}}[\mathrm{Ca}^{2+}]_{\mathrm{m,i,j,k}}[\mathrm{D}]_{\mathrm{m,i,j,k}} - k_{\mathrm{off,CaP}}[\mathrm{CaD}]_{\mathrm{m,i,j,k}} \quad (59)$$

We thank Dr. Jay D. Humphrey for help with initiating this project and Dr. Christian von Kerczek for support and advice throughout the project. This work was carried out in partial fulfillment of the requirements for the Ph.D. degree of Y.-H.J. in the Department of Mechanical Engineering, College of Engineering, University of Maryland Baltimore County, Maryland and was supported by research grants from the National Institutes of Health (R01-NS23346 to M.F.S. and R01-AR44197 to M.G.K.).

REFERENCES

Aidley, D. J. 1978. The Physiology of Excitable Cells. Cambridge University Press, Cambridge, London, U.K. 211–263.

Alberts, B., D. Bray, J. Lewis, M. Raff, K. Roberts, and J. D. Watson. 1989. Molecular Biology of the Cell. 2nd ed. Garland Publishing, Inc., New York. 847–855.

Atkinson, K. E. 1989. An Introduction to Numerical Analysis. 2nd ed. John Wiley & Sons, New York. 341–356.

Baylor, S. M., W. K. Chandler, and M. W. Marshall. 1983. Sarcoplasmic reticulum calcium release in frog skeletal muscle fibers estimated from arsenazo III calcium transients. *J. Physiol.* 344:625–666.

Baylor, S. M., and S. Hollingworth. 1998. Model of sarcomeric Ca^{2+} movements, including ATP Ca^{2+} binding and diffusion, during activation of frog skeletal muscle. *J. Gen. Physiol.* 112:297–316.

Blatter, L. A., J. Hüser, and E. Ríos. 1997. Sarcoplasmic reticulum Ca^{2+} release flux underlying Ca^{2+} sparks in cardiac muscle. *Proc. Natl. Acad. Sci. USA.* 94:4176–4181.

Blumenfeld, H., L. Zablow, and B. Sabatini. 1992. Evaluation of cellular mechanisms for modulation of calcium transients using a mathematical model of fura-2 Ca^{2+} imaging in aplysia sensory neurons. *Biophys. J.* 63:1146–1164.

Brum, G., E. Ríos, and E. Stefani. 1988. Effects of extracellular calcium on calcium movements of excitation-contraction coupling in frog skeletal muscle fibres. *J. Physiol.* 398:441–473.

Cannell, M. B., and D. G. Allen. 1984. Model of calcium movements during activation in the sarcomere of frog skeletal muscle. *Biophys. J.* 45:913–925.

Cannell, M. B., and C. Soeller. 1997. Numerical analysis of ryanodine receptor activation by L-type channel activity in the cardiac muscle diad. *Biophys. J.* 73:112–122.

Chapra, S. C., and R. P. Canale. 1988. Numerical Methods for Engineers. 2nd ed. McGraw-Hill Book Company, New York. 735–736.

Cheng, H., W. J. Lederer, and M. B. Cannell. 1993. Calcium sparks: elementary events underlying excitation-contraction coupling in heart muscle. *Science.* 262:740–744.

Crank, J. 1975. The Mathematics of Diffusion. 2nd ed. Oxford University Press, London, U.K. 4 and 29.

Escobar, A. L., P. Velez, A. M. Kim, F. Cifuentes, M. Fill, and J. L. Vergara. 1997. Kinetic properties of DM-nitrophen and calcium indicators: rapid transient response to flash photolysis. *Pflügers Arch.-Eur. J. Physiol.* 434:615–631.

Hall, J. D., S. Betarbet, and F. Jaramillo. 1997. Endogenous buffers limit the spread of free calcium in hair cells. *Biophys. J.* 73:1243–1252.

Harkins, A. B., N. Kurebayashi, and S. M. Baylor. 1993. Resting myoplasmic free calcium in frog skeletal muscle fibers estimated with fluo-3. *Biophys. J.* 65:865–881.

Holmes, T. J., S. Bhattacharyya, J. A. Cooper, D. Hanzel, V. Krishnamurthi, W. Lin, B. Koysam, D. H. Szarowski, and J. N. Turner. 1995. Light microscope images reconstructed by maximum likelihood deconvolution. *In* Handbook of Biological Confocal Microscopy. J. B. Pawley, editor. Plenum Publishing Company, New York. 389–402.

Inesi, G., and L. de Meis. 1989. Regulation of steady state filling in sarcoplasmic reticulum. *J. Biol. Chem.* 264:5929–5936.

Kargacin, G. 1994. Calcium signaling in restricted diffusion spaces. *Biophys. J.* 67:262–272.

Kargacin, G., and F. S. Fay. 1991. Ca^{2+} movement in smooth muscle cells studied with one- and two-dimensional diffusion models. *Biophys. J.* 60:1088–1100.

Klein, M. G., H. Cheng, L. F. Santana, Y.-H. Jiang, W. J. Lederer, and M. F. Schneider. 1996. Two mechanisms of quantized calcium release in skeletal muscle. *Nature.* 379:455–458.

Klein, M. G., L. Kovacs, B. J. Simon, and M. F. Schneider. 1991. Decline of myoplasmic Ca^{2+}, recovery of calcium release and sarcoplasmic Ca^{2+} pump properties in frog skeletal muscle. *J. Physiol.* 414:639–671.

Klein, M. G., A. Lacampagne, and M. F. Schneider. 1999. A repetative mode of activation of discrete Ca^{2+} release events in frog skeletal muscle fibers. *J. Physiol.* 515:391–411.

Klein, M. G., A. Lacampagne, and M. F. Schneider. 1997. Voltage dependence of the pattern and frequency of discrete Ca^{2+} release events after brief repriming in frog skeletal muscle. *Proc. Natl. Acad. Sci. USA.* 94:11061–11066.

Kushmerick, M. J., and R. J. Podolsky. 1969. Ionic mobility in muscle cells. *Science.* 166:1297–1298.

Lacampagne, A., M. G. Klein, and M. F. Schneider. 1998. Modulation of the frequency of spontaneous sarcoplasmic reticulum Ca^{2+} release events (Ca^{2+} sparks) by myoplasmic [Mg^{2+}] in frog skeletal muscle. *J. Gen. Physiol.* 111:207–224.

Lacampagne, A., W. J. Lederer, M. F. Schneider, and M. G. Klein. 1996. Repriming and activation alter the frequency of stereotyped discrete Ca^{2+} release events in frog skeletal muscle. *J. Physiol.* 497:581–588.

Lacampagne, A., C. W. Ward, M. G. Klein, and M. F. Schneider. 1999. Time course of individual Ca^{2+} sparks in frog skeletal muscle recording at high time resolution. *J. Gen. Physiol.* 113:187–198.

Mejía-Alverez, R., C. Kettlun, E. Ríos, M. D. Stern, and M. Fill. 1999. Unitary Ca^{2+} current through cardiac ryanodine receptor channels under quasi-physiological ionic conditions. *J. Gen. Physiol.* 113:177–186.

Melzer, W., E. Ríos, and M. F. Schneider. 1986. The removal of myoplasmic free calcium following calcium release in frog skeletal muscle. *J. Physiol.* 372:261–292.

Melzer, W., E. Ríos, and M. F. Schneider. 1987. A general procedure for determining the rate of calcium release from the sarcoplasmic reticulum in skeletal muscle fibers. *Biophys. J.* 51:849–863.

Pawley, J. 1995. Fundamental limits in confocal microscopy. *In* Handbook of Biological Confocal Microscopy. J. B. Pawley, editor. Plenum Publishing Company, New York. 19–37.

Peachey, L. D. 1965. The sarcoplasmic reticulum and transverse tubules of the frog's sartorius. *J. Cell Biol.* 25:209–231.

Pozrikidis, C. 1997. Introduction to Theoretical and Computational Fluid Dynamics. Oxford University Press, New York. 564.

Pratusevich, V. R., and W. Balke. 1996. Factor shaping the confocal image of the calcium spark in cardiac muscle cells. *Biophys. J.* 71:2942–2957.

Ríos, E., M. D. Stern, A. González, and N. Shirokova. 1998. Release flux underlying Ca^{2+} sparks in frog skeletal muscle. *Biophys. J.* 74:A234.

Schneider, M. F., and M. G. Klein. 1996. Sarcomeric calcium sparks activated by fiber depolarization and by cytosolic Ca^{2+} in skeletal muscle. *Cell Calcium.* 20:123–128.

Shirokova, N., and E. Ríos. 1997. Small event Ca^{2+} release: a probable precursor of Ca^{2+} sparks in frog skeletal muscle. *J. Physiol.* 502:3–11.

Sinha, S. R., L.-G. Wu, and P. Saggau. 1997. Presynaptic calcium dynamics and transmitter release evoked by single action potentials at mammalian central synapses. *Biophys. J.* 72:637–651.

Soeller, C., and M. B. Cannell. 1997. Numerical simulation of local calcium movements during L-type calcium channel gating in the cardiac diad. *Biophys. J.* 73:97–111.

Sun, X.-P., N. Callamaras, J. S. Marchant, and I. Parker. 1998. A continuum of Ins P_3-mediated elementary Ca^{2+} signalling events in *Xenopus* oocytes. *J. Physiol.* 509:67–80.

Tsugorka, A., E. Ríos, and L. A. Blatter. 1995. Imaging elementary events of calcium release in skeletal muscle cells. *Science.* 269:1723–1726.